A THREE-DIMENSIONAL MODEL FOR ESTUARIES AND COASTAL SEAS: VOLUME I, PRINCIPLES OF COMPUTATION

PREPARED FOR THE OFFICE OF WATER RESOURCES RESEARCH, DEPARTMENT OF THE INTERIOR

JAN J. LEENDERTSE
RICHARD C. ALEXANDER
SHIAO-KUNG LIU

R-1417-OWRR
DECEMBER 1973

The work upon which this publication is based was supported wholly by funds provided by the United States Department of the Interior as authorized under the Water Resources Research Act of 1964, Public Law 88-379, as amended.

Rand
SANTA MONICA, CA. 90406

A THREE-DIMENSIONAL MODEL FOR ESTUARIES AND COASTAL SEAS: VOLUME I, PRINCIPLES OF COMPUTATION

PREPARED FOR THE OFFICE OF WATER
RESOURCES RESEARCH, DEPARTMENT OF THE INTERIOR

JAN J. LEENDERTSE
RICHARD C. ALEXANDER
SHIAO-KUNG LIU

R-1417-OWRR
DECEMBER 1973

The work upon which this publication is based was supported wholly by funds provided by the United States Department of the Interior as authorized under the Water Resources Research Act of 1964, Public Law 88-379, as amended.

Rand
SANTA MONICA, CA. 90406

PREFACE

The study presented here is considered the first step toward the design of a tool for a quantitative analysis of planning for water-resource development and water-quality management of estuaries, coastal bays, and lakes.

This report lays the foundation for the development of a system to be used for numerical simulation of the fluid flow in water bodies with irregular boundaries and nonisotropic density distributions. The work is not finished, but has advanced sufficiently to show that practical applications can be made, and it also permits some judgment of its use.

SUMMARY

This report describes the principles of computation for a three-dimensional model of estuaries, bays, and coastal seas in which non-isotropic density conditions exist. Numerical integration of the finite difference equations for motion, transport, and continuity are used. In these equations the vertical momentum exchange is quadratically related to horizontal velocities, and the effects of vertical accelerations are neglected.

The computational method has been tested on a number of basins with boundaries of increasing complexity. A computation for a large lake with irregular boundaries and depth with a horizontal grid of 1000 points and 8 layers took 30 minutes on an IBM 360-91 for a real-time simulation of 67 hours in 4000 time steps.

Results indicate that three-dimensional flows can be computed effectively according to the method described in this report.

ACKNOWLEDGMENT

Our Rand colleague, A. B. Nelson, capably performed the programming for the model described in this report.

CONTENTS

PREFACE iii

SUMMARY v

ACKNOWLEDGMENT vii

Section
I. INTRODUCTION 1

II. PHYSICAL PROCESSES 3
Boundary Stress Specifications 12
Equation of State 14

III. FINITE DIFFERENCE FORMULATION 15
Grid Structure 15
The Finite Difference Approximations 17
Boundary Stress and Interfacial Stress Term Formulations 19
Integration Procedure 20

IV. COMPUTATIONAL TESTS AND RESULTS 22
Initial Test -- Uninodal Standing Oscillation 22
Wind Driven Circulations 25
Three-Dimensional Wind-Driven Circulation 31
A Perturbed Density Field 40
Systems with Irregular Boundaries 40

V. DISCUSSION 48

VI. CONCLUSIONS AND RECOMMENDATIONS 53

Appendix
EXPANSION OF A MOMENTUM EQUATION 54

REFERENCES 57

I. INTRODUCTION

Assessing proposed changes in estuaries requires the prediction of the water motions and distribution of discharged substances resulting from such changes. At present, such predictions can be made only for particular types of estuaries, not considering physical simulation on a reduced scale, with its well-known limitations.

Most estuaries and also many other large surface water bodies exhibit a three-dimensional flow structure and contain water with variable densities in all directions. The simulation of the water motions in such bodies through numerical solution of the basic hydrodynamic equations has not yet been accomplished.

Many problems must be overcome before this goal can be reached. For example, the fluid flow equations have to be formulated in a form that allows the establishment of finite difference approximations with a high order of accuracy. In addition, parametric expressions have to be introduced that are commensurate with the energy dissipation by turbulence. Also, these expressions should preferably be comparable with those already in use for solving less complicated fluid flow engineering problems. As we are faced with fluid motions of considerable complexity in complex water bodies, particular attention should be given to computability to achieve simulations well within present computer capabilities.

The continuous fluid properties during simulation are expressed at discrete points, by which approach certain approximations are made; the approximations, however, should be chosen in a manner such that basic physical laws of the fluid should still be applicable. For example, no water should disappear from our water body just by the numerical procedures we use. The law of mass conservation is obvious, but it is also desirable to find a method that contains all the energy as far as it is not dissipated by turbulent processes. We may set the goals even higher and require that many of the statistical properties of the flow also be simulated.

The research described in this report is aimed at developing and testing the principles of computation for a numerical model of three-dimensional flow in estuaries, bays, and coastal seas.

II. PHYSICAL PROCESSES

Characteristically, the fluid motions in an estuary are predominantly horizontal. Vertical velocities do occur, however, and are important, as they characterize the vertical circulation. The change in time of the vertical velocity, thus the vertical acceleration, is extremely small, particularly if compared with the acceleration by gravity. For example, the vertical accelerations caused by the diurnal tide are about six orders of magnitude smaller than the acceleration by gravity. On this basis it seems justified to neglect these vertical accelerations, and the vertical equation of motion is then replaced by the hydrostatic assumption.

In the equations of motion in the horizontal direction we include eddy viscosity terms representing the diffusion of momentum. In estuaries, the density is influenced by the salinity and temperature; in the case studied, the density will be taken dependent only on the salinity.

With these conditions, we can write for the incompressible (but nonhomogeneous) flow:

$$\frac{\partial u}{\partial t} + \frac{\partial (uu)}{\partial x} + \frac{\partial (uv)}{\partial y} + \frac{\partial (uw)}{\partial z} - fv + \frac{1}{\rho}\frac{\partial p}{\partial x} - \frac{1}{\rho}\left(\frac{\partial \tau_{xx}}{\partial x} + \frac{\partial \tau_{xy}}{\partial y} + \frac{\partial \tau_{xz}}{\partial z}\right) = 0 \tag{1}$$

$$\frac{\partial v}{\partial t} + \frac{\partial (uv)}{\partial x} + \frac{\partial (vv)}{\partial y} + \frac{\partial (vw)}{\partial z} + fu + \frac{1}{\rho}\frac{\partial p}{\partial y} - \frac{1}{\rho}\left(\frac{\partial \tau_{yx}}{\partial x} + \frac{\partial \tau_{yy}}{\partial y} + \frac{\partial \tau_{yz}}{\partial z}\right) = 0 \tag{2}$$

$$\frac{\partial p}{\partial z} + \rho g = 0 \tag{3}$$

$$\frac{\partial u}{\partial x} + \frac{\partial v}{\partial y} + \frac{\partial w}{\partial z} = 0 \tag{4}$$

$$\frac{\partial s}{\partial t} + \frac{\partial (us)}{\partial x} + \frac{\partial (vs)}{\partial y} + \frac{\partial (ws)}{\partial z} - \frac{\partial \left(D_x \frac{\partial s}{\partial x}\right)}{\partial x} - \frac{\partial \left(D_y \frac{\partial s}{\partial y}\right)}{\partial y} - \frac{\partial \left(\kappa \frac{\partial s}{\partial z}\right)}{\partial z} = 0 \tag{5}$$

$$\rho = \bar{\rho} + \rho'(s) \tag{6}$$

where

x, y, z	Cartesian coordinates positive eastward, northward, and upward, respectively
u, v, w	Respective components of velocity
t	Time
f	Coriolis parameter
p	Pressure
s	Salinity
ρ	Density
$\bar{\rho}$	Reference density, a constant
ρ'	Departure from $\bar{\rho}$ depending on salinity
κ	Vertical diffusion coefficient
τ_{xx}, τ_{xy}, τ_{yx}, τ_{yy}, τ_{xz}, τ_{yz}	Components of the stress tensor
D_x, D_y	Horizontal diffusion coefficient

The first three equations represent the equations of motion, Eq. (4) is the equation of continuity, and Eq. (5) represents the mass balance of the salts dissolved in water. The equation of state, Eq. (6), expresses the relation between the density and the salinity.

For a more complete representation of an estuarine system, a temperature equation should also be used, together with diffusion equations of substances that are important to the analysis. These equations have the same form as Eq. (5) and need not be included in the initial investigation to determine the computational principles for an estuary.

Equations (1) through (5) introduce no internal sources of momentum, fluid, or salinity.

In estuaries, the variables can change rapidly over a short distance in the vertical direction; consequently they require a grid size that is much smaller in the vertical direction than in the horizontal direction.

In the vertical we can expect a sufficient representation at points about one meter apart, while horizontally the experience with two-dimensional computations of estuaries has shown that a representation at points 100 to 300 meters apart is sufficient.

In the vertical we may also expect sharp changes locally. To resolve these with a minimum computational effort, it would be desirable to have a grid representation over the vertical that is not necessarily at equal distance.

This can be visualized by considering the fluid motion in horizontal slices, with an exchange between these slices for the mass, momentum, and salinity. This concept will enhance the derivation of the finite difference equation.

Since considerable change over the vertical can exist in the variables, it is considered advantageous to base the model upon computations of the momentum and mass fluxes in the different layers of the system. Consequently, the system of equations, Eqs. (1) through (5), requires integration over the height of the layer. If the origin of the coordinates is taken at the mean sea level (Fig. 1), then the air-water interface $z = \zeta(x, y, t)$ includes the tides and other long waves, and this interface is the boundary for the system's upper layer. Similarly, a boundary condition exists for the bottom which defines one of the system's layers. At these boundaries the mass fluxes are zero. Only momentum is transferred -- at the surface as a driving force by wind, and at the bottom as a dissipative effect related to the local velocity.

In deriving the vertically integrated equations we used Leibnitz' rule on the derivatives of an integral.

Figure 1 shows the layout of the vertical grid for a special case. The surfaces $z = z_k$ = constant, where k is an integer, are levels separating the various layers. The latter have thicknesses h_k and are counted downward. The thickness h_1 will generally vary in space and time because of changing tide levels as well as gravity waves. The thicknesses h_2, h_3, and h_4 are constant over the region shown. The number of layers will vary from one position in the horizontal plane to another depending on the depth, but the bottom layer thickness will vary with x, y according to prescribed bottom topography.

In general, there will be $\underline{b}$ layers at a given point in the horizontal plane, and the bottom layer at that point will have specified thickness

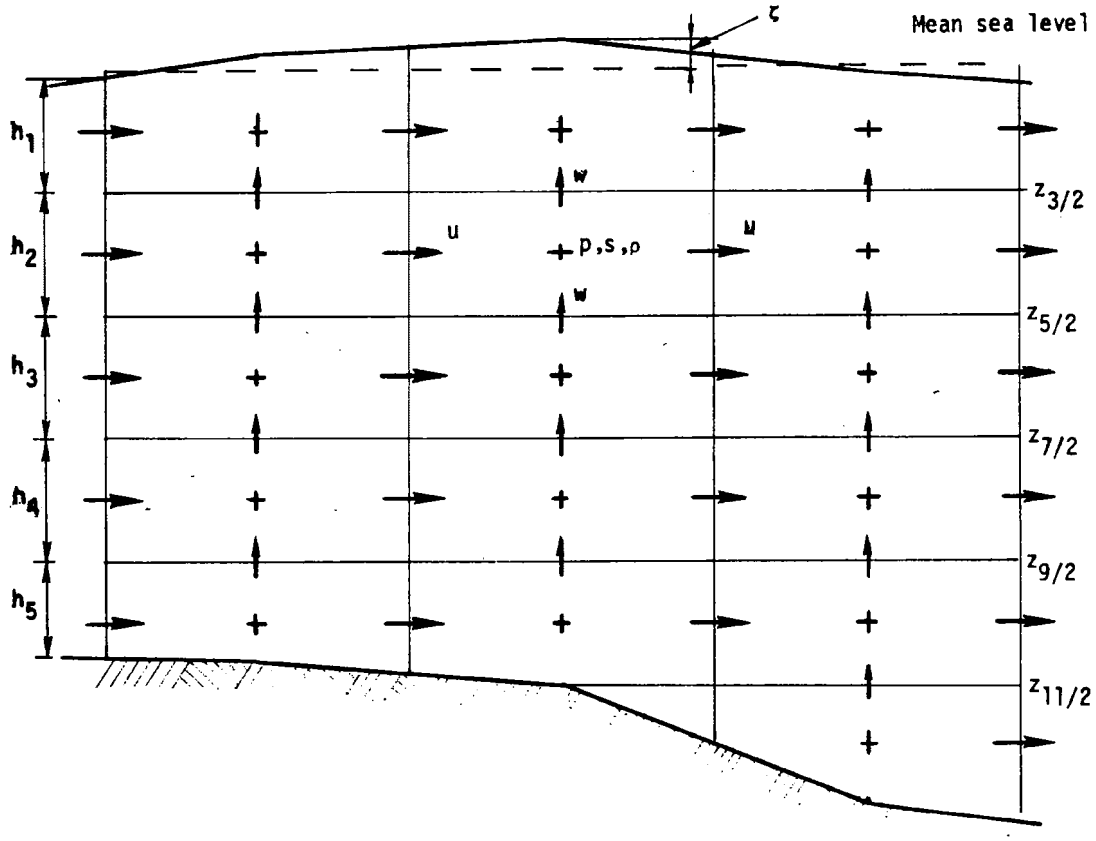

Fig. 1--Location of variables on the vertical grid

h_b. Also, in general, the intermediate layer thicknesses are not necessarily equal.

The governing equations for the mass and momentum are integrated over the kth layer, where k = 1, 2, 3, ..., b. Let

$$\langle\ \rangle_k = \int_{k+\frac{1}{2}}^{k-\frac{1}{2}} (\ )\, dz \tag{7}$$

where $k\pm\frac{1}{2}$ refers to z-levels of the interfaces between the layer k and $k\pm1$.

The vertical integration of the momentum equations, Eqs. (1) and (2), for the kth layer becomes (with subscript k in $\langle\ \rangle_k$ understood)

$$\frac{\partial\langle u\rangle}{\partial t} + \frac{\partial\langle uu\rangle}{\partial x} + \frac{\partial\langle uv\rangle}{\partial y} + (uw)_{k-\frac{1}{2}} - (uw)_{k+\frac{1}{2}}$$

$$- f\langle v\rangle + \frac{1}{\rho}\left\langle\frac{\partial p}{\partial x}\right\rangle - \frac{1}{\rho}\left[(\tau^{xz}_{k-\frac{1}{2}} - \tau^{xz}_{k+\frac{1}{2}}) + \left\langle\frac{\partial\tau_{xx}}{\partial x}\right\rangle + \left\langle\frac{\partial\tau_{xy}}{\partial y}\right\rangle\right] = 0 \tag{8}$$

$$\frac{\partial\langle v\rangle}{\partial t} + \frac{\partial\langle uv\rangle}{\partial x} + \frac{\partial\langle vv\rangle}{\partial y} + (vw)_{k-\frac{1}{2}} - (vw)_{k+\frac{1}{2}}$$

$$+ f\langle u\rangle + \frac{1}{\rho}\left\langle\frac{\partial p}{\partial y}\right\rangle - \frac{1}{\rho}\left[(\tau^{yz}_{k-\frac{1}{2}} - \tau^{yz}_{k+\frac{1}{2}}) + \left\langle\frac{\partial\tau_{yx}}{\partial x}\right\rangle + \left\langle\frac{\partial\tau_{yy}}{\partial y}\right\rangle\right] = 0 \tag{9}$$

The second and third terms in these equations represent integrals of products of velocities. These terms will be difficult to express in finite difference quotients, and the following approximations are introduced:

$$\frac{\partial\langle uu\rangle}{\partial x} \cong \frac{\partial(\frac{1}{h}\langle u\rangle\langle u\rangle)}{\partial x} \tag{10}$$

$$\frac{\partial\langle uv\rangle}{\partial y} \cong \frac{\partial(\frac{1}{h}\langle u\rangle\langle v\rangle)}{\partial y} \tag{11}$$

$$\frac{\partial \langle uv \rangle}{\partial x} \cong \frac{\partial (\frac{1}{h} \langle u \rangle \langle v \rangle)}{\partial x} \tag{12}$$

$$\frac{\partial \langle vv \rangle}{\partial y} \cong \frac{\partial (\frac{1}{h} \langle v \rangle \langle v \rangle)}{\partial y} \tag{13}$$

These approximations assume that the velocities are uniform in the vertical over the layer.

Furthermore, we can introduce the following approximations for the momentum diffusion:

$$\left(\frac{\partial \tau_{xx}}{\partial x}\right) \cong \frac{\partial \langle \tau_{xx} \rangle}{\partial x} \tag{14}$$

$$\left(\frac{\partial \tau_{xy}}{\partial y}\right) \cong \frac{\partial \langle \tau_{xy} \rangle}{\partial y} \tag{15}$$

$$\left(\frac{\partial \tau_{yx}}{\partial x}\right) \cong \frac{\partial \langle \tau_{yx} \rangle}{\partial y} \tag{16}$$

$$\left(\frac{\partial \tau_{yy}}{\partial y}\right) \cong \frac{\partial \langle \tau_{yy} \rangle}{\partial y} \tag{17}$$

The vertical pressure gradient in Eq. (3) can be approximated by

$$\frac{\bar{P}_k - P_{k+1}}{\frac{1}{2}(h_k + h_{k+1})} = -\rho_{k+\frac{1}{2}} g \tag{18}$$

where P_k is the layer-average pressure for layer **k, and** $\rho_{k+\frac{1}{2}}$ **is a** two-point average for density, defined by

$$\rho_{k+\frac{1}{2}} = \tfrac{1}{2}(P_k + P_{k+1}) \tag{19}$$

where P = layer average density.

The same principle can be extended to represent all the interface values of dependent variables as the two-point averages of the adjacent layer-averages of the same variables, e.g.,

$$u_{k+\frac{1}{2}} = \tfrac{1}{2}(U_k + U_{k+1}) \tag{20}$$

where U = layer-average velocity.

The horizontal pressure gradient term for the top layer can be approximated by

$$\left.\begin{aligned} \frac{\partial P}{\partial x} &= g\bar{\rho}\frac{\partial \zeta}{\partial x} + \tfrac{1}{2}gh_1\frac{\partial \rho_1}{\partial x} \\ \frac{\partial P}{\partial y} &= g\bar{\rho}\frac{\partial \zeta}{\partial y} + \tfrac{1}{2}gh_1\frac{\partial \rho_1}{\partial y} \end{aligned}\right\} k = 1 \tag{21}$$

The pressure gradient for the other layers is, according to Eq. (18),

$$\left.\begin{aligned} \frac{\partial P_k}{\partial x} &= \frac{\partial P_{k-1}}{\partial x} + gh_{k-\frac{1}{2}}\frac{\partial \rho_{k-\frac{1}{2}}}{\partial x} \\ \frac{\partial P_k}{\partial y} &= \frac{\partial P_{k-1}}{\partial y} + gh_{k-\frac{1}{2}}\frac{\partial \rho_{k-\frac{1}{2}}}{\partial y} \end{aligned}\right\} k = 2, 3 \ldots b \tag{22}$$

In the following, for the sake of convenience, we revert back to the original notation for variables, i.e., U_k, V_k, P_k, ρ_k, and S_k are replaced by u_k, v_k, p_k, ρ_k, and s_k, respectively. Integer subscript k will be used to distinguish layer averages from interface values, the latter being designated by $k+\frac{1}{2}$. For example,

$$u_k = \frac{1}{h_k}\int_{k+\frac{1}{2}}^{k-\frac{1}{2}} u(x, y, z, t)\, dz \tag{23}$$

but

$$u_{k+\frac{1}{2}} = [u(x, y, z, t)]_{z=z_{k+\frac{1}{2}}} \tag{24}$$

When the continuity equation is integrated over layer k, i.e.,

$$\int_{k+\frac{1}{2}}^{k-\frac{1}{2}} \left(\frac{\partial w}{\partial z} + \frac{\partial u}{\partial x} + \frac{\partial v}{\partial y}\right) dz = 0 \tag{25}$$

then

$$w_{k-\frac{1}{2}} - w_{k+\frac{1}{2}} + \int_{k+\frac{1}{2}}^{k-\frac{1}{2}} \left(\frac{\partial u}{\partial x} + \frac{\partial v}{\partial y}\right) dz = 0 \tag{26}$$

Interchanging the differential operator $\frac{\partial}{\partial x} + \frac{\partial}{\partial y}$ and $\int dz$, and accounting for the limits of integration, gives the vertical velocity component w at the interface k-½:

$$w_{k-\frac{1}{2}} = -\sum_{\ell=k}^{b} \left\{\frac{\partial (hu)}{\partial x} + \frac{\partial (hv)}{\partial y}\right\} \tag{27}$$

Equation (27) is the equation of continuity in differential form for a layer k. At the water surface, the continuity equation reduces to

$$\frac{\partial \zeta}{\partial t} + \sum_{\ell=1}^{b} \left\{\frac{\partial (hu)}{\partial x} + \frac{\partial (hv)}{\partial y}\right\} = 0 \tag{28}$$

In Eqs. (8) and (9), shear stresses resulting from the vertical gradient of horizontal velocity components are expressed as τ^{xz} and τ^{yz} terms. Parametric expressions for these interfacial and boundary stresses will be described later. Horizontal momentum diffusion terms in Eqs. (8) and (9) are expressed as gradients of Reynolds stresses, and they are evaluated by means of eddy viscosity coefficients A through the relationships

$$\tau_{xx} = A_{xx} \frac{\partial u}{\partial x}, \qquad \tau_{xy} = A_{xy} \frac{\partial u}{\partial y} \tag{29)(30}$$

$$\tau_{yy} = A_{yy} \frac{\partial v}{\partial y}, \qquad \tau_{yx} = A_{yx} \frac{\partial v}{\partial x} \tag{31)(32}$$

A further approximation for developing a computational scheme is the use of

$$\tau_{xx} = A_x \frac{\partial u}{\partial x} \tag{33}$$

$$\tau_{xy} = A_x \frac{\partial u}{\partial y} \tag{34}$$

$$\tau_{yx} = A_y \frac{\partial v}{\partial x} \tag{35}$$

$$\tau_{yy} = A_y \frac{\partial v}{\partial y} \tag{36}$$

With u, v, p, and s representing the layer averages of a particular layer k, and $k\pm\frac{1}{2}$ as a subscript designating interface values of that layer, the equations of motion become

$$\frac{\partial(hu)}{\partial t} + \frac{\partial(huu)}{\partial x} + \frac{\partial(hvu)}{\partial y} + (wu)_{k-\frac{1}{2}} - (wu)_{k+\frac{1}{2}}$$

$$- fhv + \frac{h}{\rho}\frac{\partial p}{\partial x} + \left(\frac{1}{\rho}\tau^{xz}\right)_{k+\frac{1}{2}} - \left(\frac{1}{\rho}\tau^{xz}\right)_{k-\frac{1}{2}} - \frac{1}{\rho}\frac{\partial(hA_x\frac{\partial u}{\partial x})}{\partial x} - \frac{1}{\rho}\frac{\partial(hA_y\frac{\partial u}{\partial y})}{\partial y} = 0 \tag{37}$$

$$\frac{\partial(hv)}{\partial t} + \frac{\partial(hvu)}{\partial x} + \frac{\partial(hvv)}{\partial y} + (wv)_{k-\frac{1}{2}} - (wv)_{k+\frac{1}{2}}$$

$$+ fhu + \frac{h}{\rho}\frac{\partial p}{\partial y} + \left(\frac{1}{\rho}\tau^{yz}\right)_{k+\frac{1}{2}} - \left(\frac{1}{\rho}\tau^{yz}\right)_{k-\frac{1}{2}} - \frac{1}{\rho}\frac{\partial(hA_x\frac{\partial v}{\partial x})}{\partial x} - \frac{1}{\rho}\frac{\partial(hA_y\frac{\partial v}{\partial y})}{\partial y} = 0 \tag{38}$$

$$\frac{\partial(hs)}{\partial t} + \frac{\partial(hus)}{\partial x} + \frac{\partial(hvs)}{\partial y} + (ws)_{k-\frac{1}{2}} - (ws)_{k+\frac{1}{2}}$$

$$- \frac{\partial(hD_x\frac{\partial s}{\partial x})}{\partial x} - \frac{\partial(hD_y\frac{\partial s}{\partial y})}{\partial y} + (\kappa\frac{\partial s}{\partial z})_{k+\frac{1}{2}} - (\kappa\frac{\partial s}{\partial z})_{k-\frac{1}{2}} = 0 \tag{39}$$

BOUNDARY STRESS SPECIFICATIONS

Two of the major sources and sinks of energy to an estuary system are wind stress from the upper boundary and the dissipative stresses from bottom friction. The characteristics of these two mechanisms are not of the same nature; they are relatively similar, however, as opposed to the interfacial shear stress components generated from the vertical velocity gradient within the main body of water.

An estuarine water surface under the movement of air is basically different from a solid boundary because a fluid interface cannot support a stress discontinuity. The water surface is characterized by traveling waves that derive their momentum from the wind through wave-generating mechanisms. This macroscopic wind-wave interactive system is beyond the resolving power of the basic simulation grid size. Similarly, the interaction between the moving water immediately above the movable bed of an estuary and the sediment transport mechanism is also beyond the resolving capability of the simulation grid size. The gross effects of the two above-mentioned mechanisms have to be accounted for and incorporated in the simulation by means of parametric expressions.

Both the air-water and water-sediment interfaces are characterized by their density differences between the two couplings. Difficulties in deriving an explicit parametric expression for these two types of interaction come from the fact that both heavier, dependent media cannot completely sustain shear stresses as if they were solid, nonmovable boundaries as in the case of pipe walls to the moving fluid within them. The logarithmic velocity distribution gives rise to the possibility of determining the boundary stress from the knowledge of a roughness parameter and the measurement of fluid speed. The relationship is the commonly known quadratic law:

$$\tau_o = \rho C \, \bar{u}|\bar{u}| \tag{40}$$

where ρ is the density of the moving fluid,

$\bar{u}$ is the mean wind speed, and

C is a drag coefficient.

The validity of using the quadratic law for estimating shear stresses

at water surface and fluid above a movable sediment bed has been a controversial matter for many years. However, recent works by Neumann,[1] Miles,[2] Phillips,[3] and Stewart[4] on the momentum transfer from turbulent wind to surface waves, and on the wave-induced Reynolds stress, show that in statistically steady and neutral stability conditions, the measured wind profile near the wavy surface should be logarithmic. In addition, Phillips[3] showed that themmean properties of the boundary layer determined with measurements from fixed probes (say, at 10-meter anemometric height) should be comparable to those over a solid boundary.

From the above argument, we can apply the quadratic expression for estimating both the surface wind-induced stress and the bottom current-induced drag. The horizontal wind stress components τ_x^s and τ_y^s are expressed as functions of the wind velocity and air density.

$$\tau_x^s = C^* \rho_a w^2 \sin \psi \tag{41}$$

$$\tau_y^s = C^* \rho_a w^2 \cos \psi \tag{42}$$

where ρ_a is the atmospheric density, w is the wind speed at 10-meter level, ψ is the angle between the wind direction and the y-axis, and C^*, the resistance coefficient. The latter was set at 2.6×10^{-3} for all the test computations.

The bottom stresses can be estimated by another quadratic expression:

$$\tau_x^b = a\rho_w u\sqrt{u^2 + v^2} \tag{43}$$

$$\tau_y^b = a\rho_w v\sqrt{u^2 + v^2} \tag{44}$$

where a is a dimensionless resistance parameter that may depend on the boundary roughness and on the Reynolds number, ρ_w is the density of water at the bottom layer, and u, v are horizontal velocity components at the bottom layer.

If we let $C = \sqrt{g/a}$, the horizontal shear stress components at the bottom are

$$\tau_x^b = \rho_w g \frac{u\sqrt{u^2 + v^2}}{C^2} \tag{45}$$

$$\tau_y^b = \rho_w g \frac{v\sqrt{u^2 + v^2}}{C^2} \tag{46}$$

where C is a Chezy's coefficient, which is dependent on the layer thickness.

EQUATION OF STATE

In order to evaluate the pressure gradient terms in the equations of motion, the density field has to be determined. The density ρ (mass per unit volume) or the specific volume α ($= \frac{1}{\rho}$) of estuarine water (ranges from the relatively fresh river water to the more dense, saline coastal ocean water) depends on temperature T, salinity s, and, in a strict sense, depends also on the pressure as a result of the slight compressibility of waterr. This relationship can be described according to Eckart[5] from the Tumlirz equation of state given by

$$(p + p_o)(\alpha - \alpha_o) = \lambda \tag{47}$$

where p = pressure, α = specific volume, and p_o and α_o are empirical functions of temperature. Since the effect of pressure on density is negligible for the water depth concerned, Eq. (47) can be simplified as

$$\rho = \frac{1}{\alpha} = \frac{p_o}{\lambda + \alpha_o p_o} \tag{48}$$

and, according to Eckart,

$$\lambda = 1779.5 + 11.25T - .0745T^2 - (3.80 + .01T)s \tag{49}$$

$$\alpha_o = .6980 \tag{50}$$

$$p_o = 5890 + 38T - .375T^2 + 3s \tag{51}$$

Since the numerical values of estuarine water density always start with 1.0 ... to avoid large errors in calculating density gradients, the density departure ρ' (from a mean $\bar{\rho}$, say 1.000) will be used.

III. FINITE DIFFERENCE FORMULATION

GRID STRUCTURE

Equations (37) through (39) permit various finite-difference approximations. A space-staggered grid was selected.

This representation has the advantage that in the momentum equations the pressure term is described by a simple central quotient in relation to the velocity, and in the continuity equations the mass-flux gradients are described by simple central quotients (Fig. 2). With this grid, the advection terms can be expressed in a form such that conservation of energy in the horizontal motions can be achieved, as discussed in Section IV.

The grid structure is the same as used in a two-dimensional model for estuaries (Leendertse)[6] except for the location of depth values, and is also the same as used by Lilly for two-dimensional computations of a baratropic fluid. Since a three-dimensional computational model is designed, a number of these grids, as shown in Fig. 2, will be located above each other.

The pressure p and the salinity s are computed at integer values of i, j, and k. The velocities u are computed at half-integer values of i and integer values of j and k, and the velocities v are computed at integer values of i and k, and half-integer values of j.

The velocities w are computed at integer values of i and j, and half-integer values of k. The latter is located at the interfaces of the slices discussed earlier. The relative position of the variables in space is shown in Fig. 3.

If the thickness of the slice is taken as a constant, then the w velocity is expressed as central between the location of the pressures. The water surface elevation is expressed only at a two-dimensional horizontal grid and has integer values of i and j.

The formulation of a finite difference scheme using expressions containing the differences or products of the individual values of indexed variables is very cumbersome.

Shuman[7] introduces sum and difference operations as an aid in

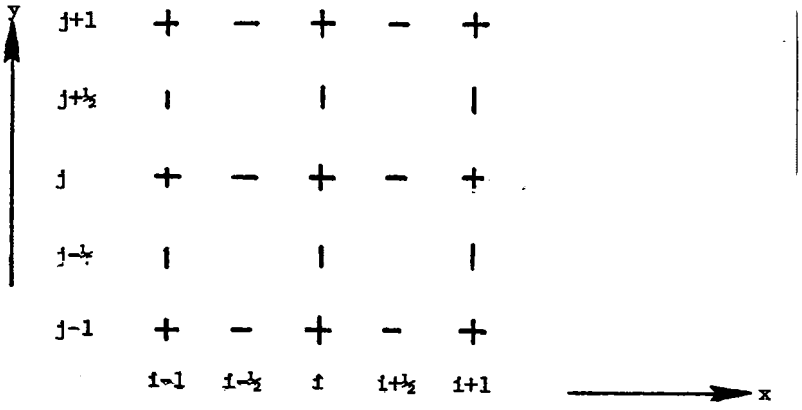

Fig. 2--The location of u (—), v (|), and other parameters (+) in the space-staggered grid

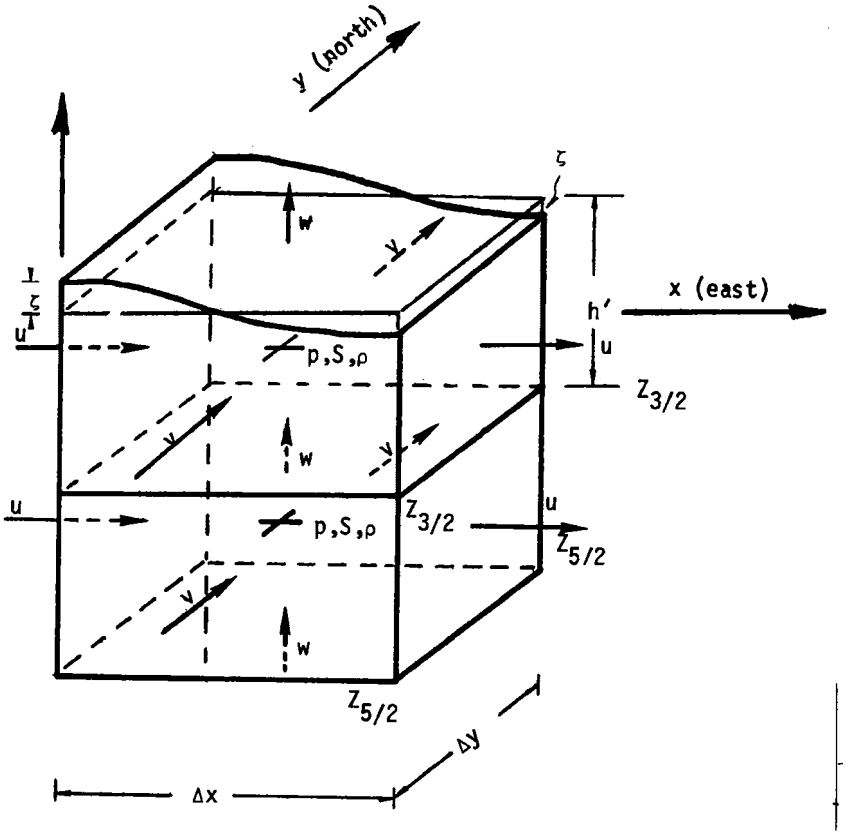

Fig. 3--Relative position of the variables in the model

formulating a finite difference scheme and this formulation will be used in this report with some extensions for indicating time levels. For example, for an arbitrary variable F,

$$F \equiv F(i\Delta x, j\Delta y, k\Delta z, n\Delta t)$$

where the position coordinate in the horizontal plane is determined on the finite difference grid by

$$(i\Delta x, j\Delta y) \text{ and } i,j = 0, \pm 1/2, 1, 3/2, \ldots$$

The vertical position is determined as to its location in the center of the layer numbered from the top with integer $k = 1, 2, 3 \ldots$ or at the horizontal interfaces with half-integer values $k = 1/2, 3/2, 5/2 \ldots$

Time is determined by the number of time steps ($n\Delta t$) from the reference time, with n an integer value.

The following sum and difference operators are adopted:

$$\overline{F}^{x} = \tfrac{1}{2}\left\{F[(i + \tfrac{1}{2})\,\Delta x, j\Delta y, k\Delta z, n\Delta t] + F[(i - \tfrac{1}{2})\,\Delta x, j\Delta y, k\Delta z, n\Delta t]\right\} \quad (52)$$

$$\delta_x F = \frac{1}{\Delta x}\left\{F[(i + \tfrac{1}{2})\,\Delta x, j\Delta y, k\Delta z, n\Delta t] - F[(i - \tfrac{1}{2})\Delta x, j\Delta y, k\Delta z, n\Delta t]\right\} \quad (53)$$

These are shown only for x, but are also used for y, z, and t.

The special notation used for shifted time levels is

$$F_{+} = F[i\Delta x, j\Delta y, k\Delta z, (n + 1)\Delta t] \quad (54)$$

$$F_{-} = F[i\Delta x, j\Delta y, k\Delta z, (n - 1)\Delta t] \quad (55)$$

THE FINITE DIFFERENCE APPROXIMATIONS

The finite difference approximations of Eq. (28) and Eqs. (37) through (39) are all presented at the level k, and are expressed in vertical averaged values over the layer or slice k, as far as related to the horizontal motions. The finite difference approximations used for integration follow:

$$\overline{\delta_t \zeta}^t = -\sum_k \left\{ \delta_x(\overline{h}^x u) + \delta_y(\overline{h}^y v) \right\} \qquad \text{at } i, j, n \tag{56}$$

$$\overline{\delta_t(\overline{h}^x u)}^t = -\delta_x(\overline{\overline{h}^x u\, \overline{u}^x}^x) - \delta_y(\overline{\overline{h}^y v\, \overline{u}^y}^x) - \overline{h}^x \delta_z(\overline{u^z w}^x)$$
$$+ f\overline{h}^x \overline{v}^{xy} - \frac{1}{\overline{\rho}^x} \overline{h}^x \delta_x p - \left(\frac{1}{\overline{\rho}^{xz}} \tau^{xz}\right)_{k+\frac{1}{2}} + \left(\frac{1}{\overline{\rho}^{xz}} \tau^{xz}\right)_{k-\frac{1}{2}}$$
$$+ \frac{1}{\overline{\rho}^x}\left[\delta_x\left\{\overline{\overline{h}^x A_x}^x \delta_x u\right\}_- + \delta_y\left\{\overline{\overline{h}^x A_y}^y \delta_y u\right\}_-\right]$$
$$\text{at } i + \tfrac{1}{2}, j, k, n \tag{57}$$

$$\overline{\delta_t(\overline{h}^y v)}^t = -\delta_x(\overline{\overline{h}^x u\, \overline{v}^y}^x) - \delta_y(\overline{\overline{h}^y v\, \overline{v}^y}^y) - \overline{h}^y \delta_z(\overline{v^z w}^y)$$
$$- f\overline{h}^y \overline{u}^{xy} - \frac{1}{\overline{\rho}^y} \overline{h}^y \delta_y p - \left(\frac{1}{\overline{\rho}^{yz}} \tau^{yz}\right)_{k+\frac{1}{2}} + \left(\frac{1}{\overline{\rho}^{yz}} \tau^{yz}\right)_{k+\frac{1}{2}}$$
$$+ \frac{1}{\overline{\rho}^y}\left[\delta_x\left\{\overline{\overline{h}^y A_x}^x \delta_x v\right\}_- + \delta_y\left\{\overline{\overline{h}^y A_y}^y \delta_y v\right\}_-\right]$$
$$\text{at } i, j + p, k, n \tag{58}$$

$$\overline{\delta_t(hs)}^t = -\delta_x(\overline{h}^x u \overline{s}^x) - \delta_y(\overline{h}^y v \overline{s}^y) - h\,\delta_z(w\overline{s}^z)_-$$
$$+ \delta_x\left\{\overline{h}^x D_x \delta_x s\right\}_- + \delta_y\left\{\overline{h}^y D_y \delta_y s\right\}_- + h\,\delta_z(\kappa \delta_z s)_-$$
$$\text{at } i, j, k, n \tag{59}$$

These finite difference equations in the compact notation which was used have the same appearance as the differential equations. This will be noted, for example, by comparing Eq. (37) with Eq. (57). The latter equation is presented in expanded form in Appendix A.

The density is computed with the equation of state described in Section II:

$$\rho = p_o/(\lambda + \alpha_o p_o) \qquad \text{at } i, j, k, n + 1 \tag{48}$$

with the functions computed by Eqs. (49), (50), and (51).

The finite difference equations used to compute derived variables are the following:

$$\delta_z w = -\delta_x(\overline{h}^x u) - \delta_y(\overline{h}^y v)$$

at i, j, k, n + 1 (60)

$$\delta_x p = g(\overline{\rho}^x \delta_x \zeta) + \tfrac{1}{2}\,\overline{h}^x \delta_x \rho$$

at i + ½, j, 1, n + 1 (61)

$$\delta_y p = g(\overline{\rho}^y \delta_y \zeta) + \tfrac{1}{2}\,\overline{h}^y \delta_y \rho$$

at i, j + ½, 1, n + 1 (62)

$$\delta_z(\delta_x p) = g\,\overline{h}^z \delta_x \overline{\rho}^z$$

at i + ½, j, k + ½, n + 1 (63)

$$\delta_z(\delta_y p) = g\,\overline{h}^z \delta_y \overline{\rho}^z$$

at i, j + ½, k + ½, n + 1 (64)

BOUNDARY STRESS AND INTERFACIAL STRESS TERM FORMULATIONS

At the surface, the stress term can be computed directly from Eqs. (41) and (42):

$$\left(\frac{1}{\overline{\rho}^{xz}}\,\tau_-^{xz}\right)_{k-\frac{1}{2}} = C^*\frac{\rho_a}{\overline{\rho}^x}\,w_a^2 \sin\phi \qquad \text{at } i + \tfrac{1}{2},\ j,\ 1,\ n \tag{65}$$

$$\left(\frac{1}{\overline{\rho}^{yz}}\,\tau_-^{yz}\right)_{k-\frac{1}{2}} = C^*\frac{\rho_a}{\overline{\rho}^y}\,w_a^2 \cos\phi \qquad \text{at } i,\ j + \tfrac{1}{2},\ 1,\ n \tag{66}$$

Similarly, the stress term at the bottom (in layer b) can be computed from Eqs. (43) and (44):

$$\left(\frac{1}{\overline{\rho}^{xz}}\,\tau_-^{xz}\right)_{k+\frac{1}{2}} = g u_- \left[u_-^2 + (\overline{v_-}^{xy})^2\right]^{\frac{1}{2}} \Big/ (\overline{C}^x)^2$$

at i + ½, j, b, n (67)

$$\left(\frac{1}{\overline{\rho}^{yz}}\,\tau_-^{yz}\right)_{k+\frac{1}{2}} = g v_- \left[(\overline{u_-}^{xy})^2 + v_-^2\right]^{\frac{1}{2}} \Big/ (\overline{C}^y)^2$$

at i, j + ½, b, n (68)

Since estuary motions are mostly turbulent, eddy viscosity effects play a significant part in controlling stresses between adjacent layers with different velocities. Mass and momentum transfer are the result, and these transfers tend to equalize relative velocity differences in both the lateral and the vertical directions. If the quadratic relationship between the interlayer stresses and the velocity differences is assumed applicable, as was the case for the boundary stress specifications described earlier, the following expressions from Eqs. (57) and (58) for the interlayer stresses can be used:

$$\left(\frac{1}{\overline{\rho}^{xz}}\,\tau^{xz}\right)_{k+\frac{1}{2}} = \nu(\delta_z u)\left[(\delta_z u)^2 + (\delta_z \overline{v}^{xy})^2\right]^{\frac{1}{2}} \qquad \text{at } i+\tfrac{1}{2},\ j,\ k+\tfrac{1}{2},\ n \tag{69}$$

$$\left(\frac{1}{\overline{\rho}^{yz}}\,\tau^{yz}\right)_{k+\frac{1}{2}} = \nu(\delta_z v)\left[(\delta_z \overline{u}^{xy})^2 + (\delta_z v)^2\right]^{\frac{1}{2}} \qquad \text{at } i,\ j+\tfrac{1}{2},\ k+\tfrac{1}{2},\ n \tag{70}$$

where τ^{xz} = component of the interfacial shear stress in x direction,
τ^{yz} = component of the interfacial shear stress in y direction,
ν = coefficient of interfacial friction.

The equations used in the numerical integrations are second order approximations in time and space, except that the evaluation of the momentum diffusion by use of Eqs. (69) and (70) in Eqs. (57) and (58) is not central in time, but at a lower time level, since otherwise the computation would become unstable. For the same reason the dispersion terms in Eq. (59) are taken at the lower time level.

INTEGRATION PROCEDURE

In describing the progress of the computation, it is assumed that the computation has progressed to a time level n. At this time the velocity components u and v, the salinity s, and the pressure p are all determined for each point of the grid and available for computation. These variables are also available at the previous time step n - 1.

The water levels are also available for computation at time level n and n - 1.

At the boundaries of the water body to be computed, all diffusion coefficients are zero, as are the velocities perpendicular to the boundary. In this manner no mass fluxes or diffusive transports of salt will result. The boundaries of the horizontal layers also satisfy a no-slip boundary condition.

With this information, the prediction equations, (56) through (59), are used to advance the computational field of ζ, u, v, and s. For the evaluation of the boundary and interfacial stress terms in these equations, use is made of Eqs. (65) through (70). These are all explicit operations for each of the variables resulting in computed values of ζ, u, v, and s at time level n + 1.

Subsequently, the vertical velocities, the densities, and the pressures required for the next step of the integration are computed. For the vertical velocity, Eq. (60) is used, starting at the bottom layer and proceeding upward with the computation. In this manner the vertical velocity at the lower interface is known and the other vertical velocity can be determined explicitly.

The density for each grid point can be computed by using Eq. (48) from the salinity data now available at time n + 1. As water levels and densities are now known at time level n + 1, the pressure gradients in the x and y directions can now be computed by using Eqs. (61) through (64). In this case, first the gradients at the surface layer are computed by using Eqs. (61) and (64), and subsequently the other layers, proceeding downward. In this manner the horizontal pressure gradient in the upper layer of the two layers involved in Eqs. (63) and (64) is known, and the horizontal pressure gradient in the lower layer can be determined explicitly.

Thereafter we are ready to repeat the computational cycle and compute ζ, u, v, and s for time level n + 2, as all variables are now determined for time level n + 1.

To start a computation, information at two time levels is required. For the sample simulations presented in the next section of the report, a single forward differencing step is used to obtain the information on the second time step.

IV. COMPUTATIONAL TESTS AND RESULTS

After we completed the basic computational code development, we used several sample cases to test the code. These simulation tests were characterized by their increasing complexities in both boundary geometrics and the hydrodynamic behavior of the processes simulated. Computer graphics were employed to show the essential aspects of the simulation. The Integrated Graphics System (IGS)[8] language developed by Rand was used to program the simulation output and to produce graphical output on 35mm film and on hardcopy using an FR-80.

INITIAL TEST--UNINODAL STANDING OSCILLATION

The initial phase of the test involves a seiche oscillation in a rectangular basin. This basin was 3400m long, 1400m wide, and 7m deep. At the beginning of the simulation ($t = 0$), the initial water surface profile was one-half a cosine wave with a maximum on the far left and a minimum on the far right end (see Fig. 4). The velocities u, v, w in the water body are zero everywhere. At this instant, all the energy of the system is stored in the form of potential energy. From this point in time, a system of currents is set up as the amplitude of the seiche decreases such that water everywhere is moving from left to right. The left-hand graph of Fig. 4 shows the instantaneous current field of the center section of the basin at the 50th simulation time step. At the first few simulation time steps, the computed results are almost identical to the analytical solution, except that the current at the bottom layer ($k = 7$) is smaller due to the bottom friction. The analytical solution exists (Neumann and Pierson, Ref. 9) for this simplest two-dimensional case of uninodal standing oscillation if the Coriolis force, the advection terms, and the interfacial and bottom friction are all neglected. The period of oscillation, according to the analytical solution, is approximately 164 time steps. The five sketches on the right-hand side of Fig. 4 show the sequential surface profiles and current field at an increment of 1/8 oscillation period. Figure 5 shows the computed time history of the horizontal current velocity components at different layers near the center section of the basin. Note that as

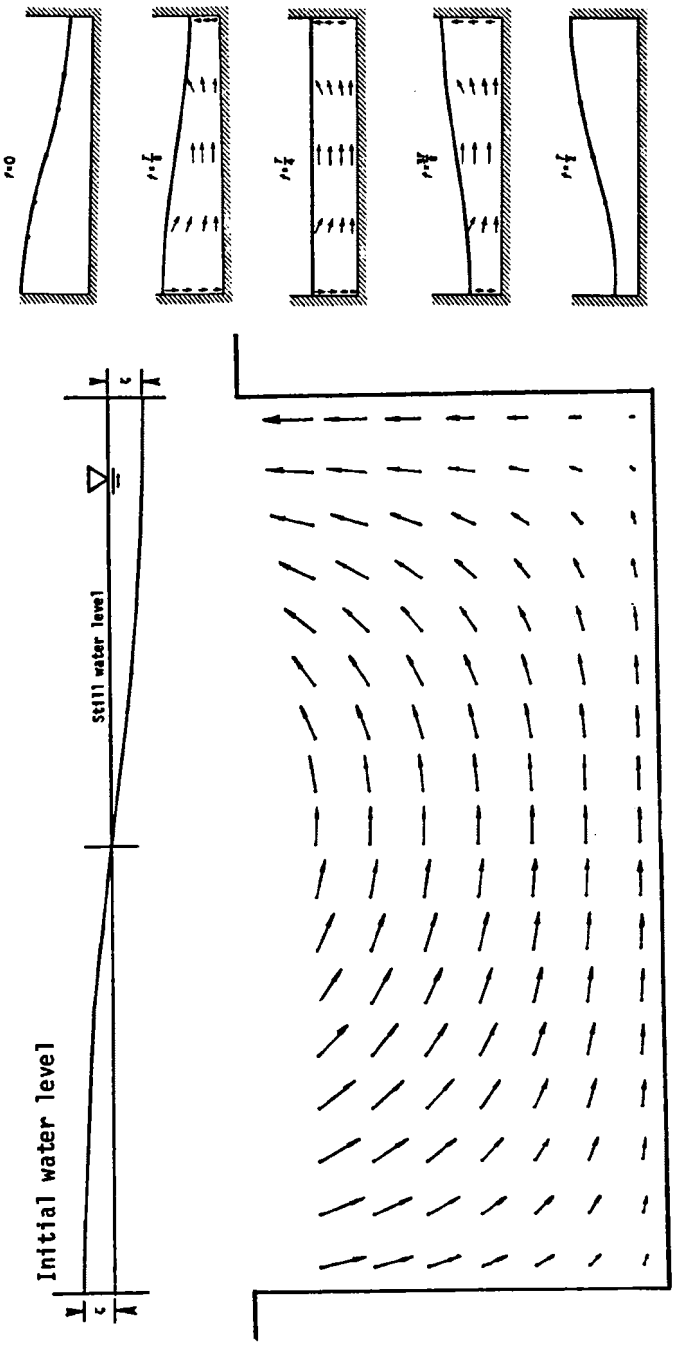

Fig. 4--A typical velocity vector field from an oscillating wave in a rectangular basin

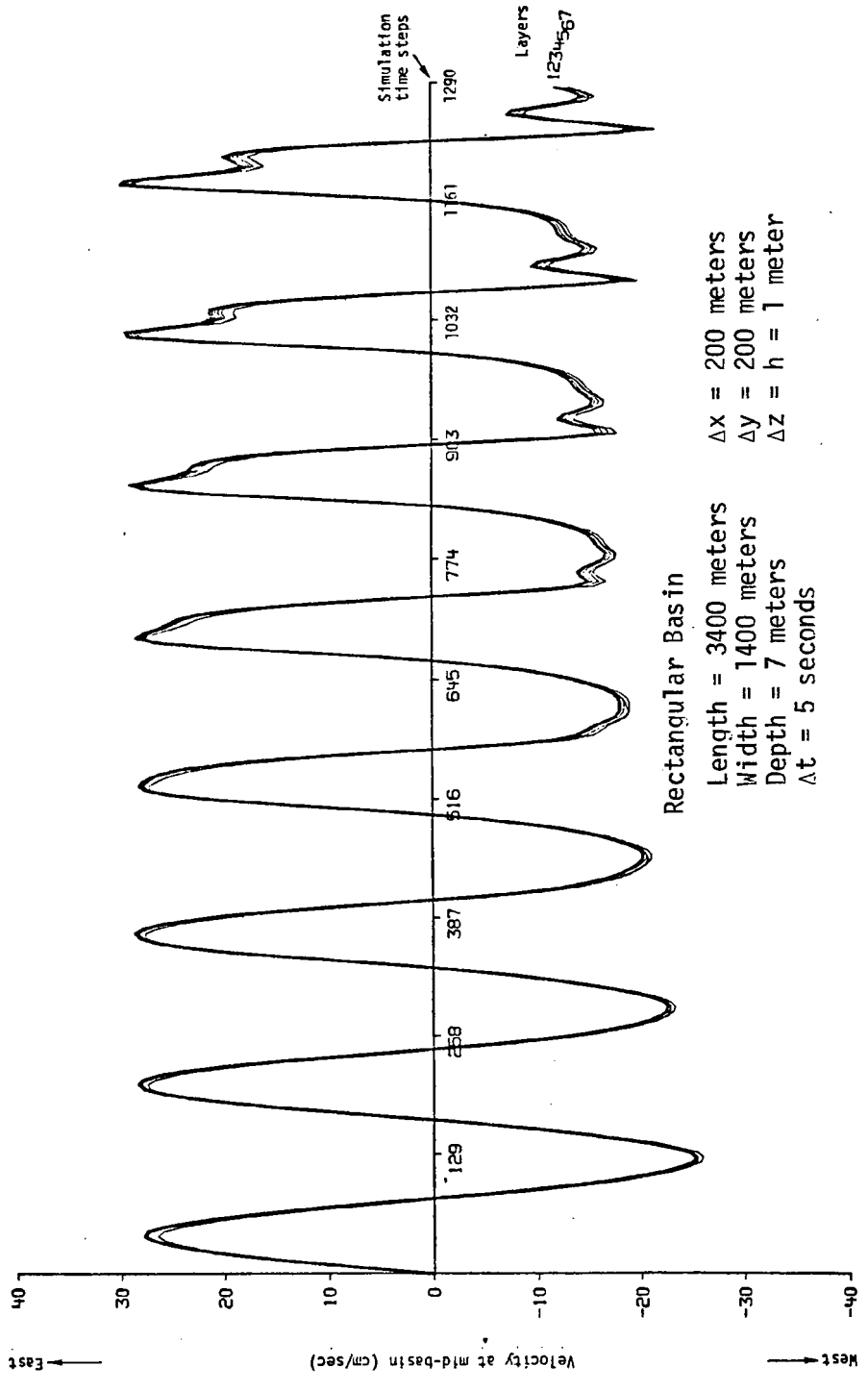

Fig. 5--Time history of the horizontal current velocity components at different layers of an oscillating wave in a rectangular basin with bottom friction (Chezy's C = 70 meters$^{\frac{1}{2}}$/sec)

time proceeds, a higher mode of oscillation starts to develop due to the nonlinear effects. Using the leapfrog scheme, simulation was carried out up to 2000 integration time steps without showing any sign of instability. The same simulation, but without Coriolis, stress, and viscosity terms in the formulation, has also been run up to 2000 steps without stability problems. This indicates that the stability of the computation is not dependent on the viscosity, as is often the case with numerical models of this type.

WIND-DRIVEN CIRCULATIONS

In this simulation series a constant wind stress is imposed on the surface of the basin for 500 time steps. During this period, a wind-driven circulation in the basin is gradually developed and finally reaches a quasi-equilibrium condition. At this time, the wind stress is removed and the system is allowed to oscillate freely in a similar fashion to the earlier test run. This free oscillation process is then allowed to continue until it is damped out gradually by the viscosity effect.

The initial test of this series involves a rectangular basin of constant depth with no salinity gradient within the system. The top of Fig. 6 shows a vertical section through the longest axis of the basin, together with characteristic dimensions of the system. The next sixteen graphs in Figs. 6 and 7 show the system's transient response under wind stress. Each graph, with the simulation time step indicated at the lower left corner, shows the sequential development of the wind-induced circulation pattern. In these graphs the vertical scale has been enlarged 200 times, and also the vertical velocity components are multiplied by 200 before the computation of the x-z velocity vectors at each grid point.

In the beginning, only a surface current is set up by the wind stress. This can be seen in the graph of the 5th time step. The next two graphs in the sequence show the penetration of surface current to the deeper layer through the viscosity and vertical advection effects, and vertical velocity components at two ends of the basin are beginning to develop. The next five graphs in the sequence (20th through 40th

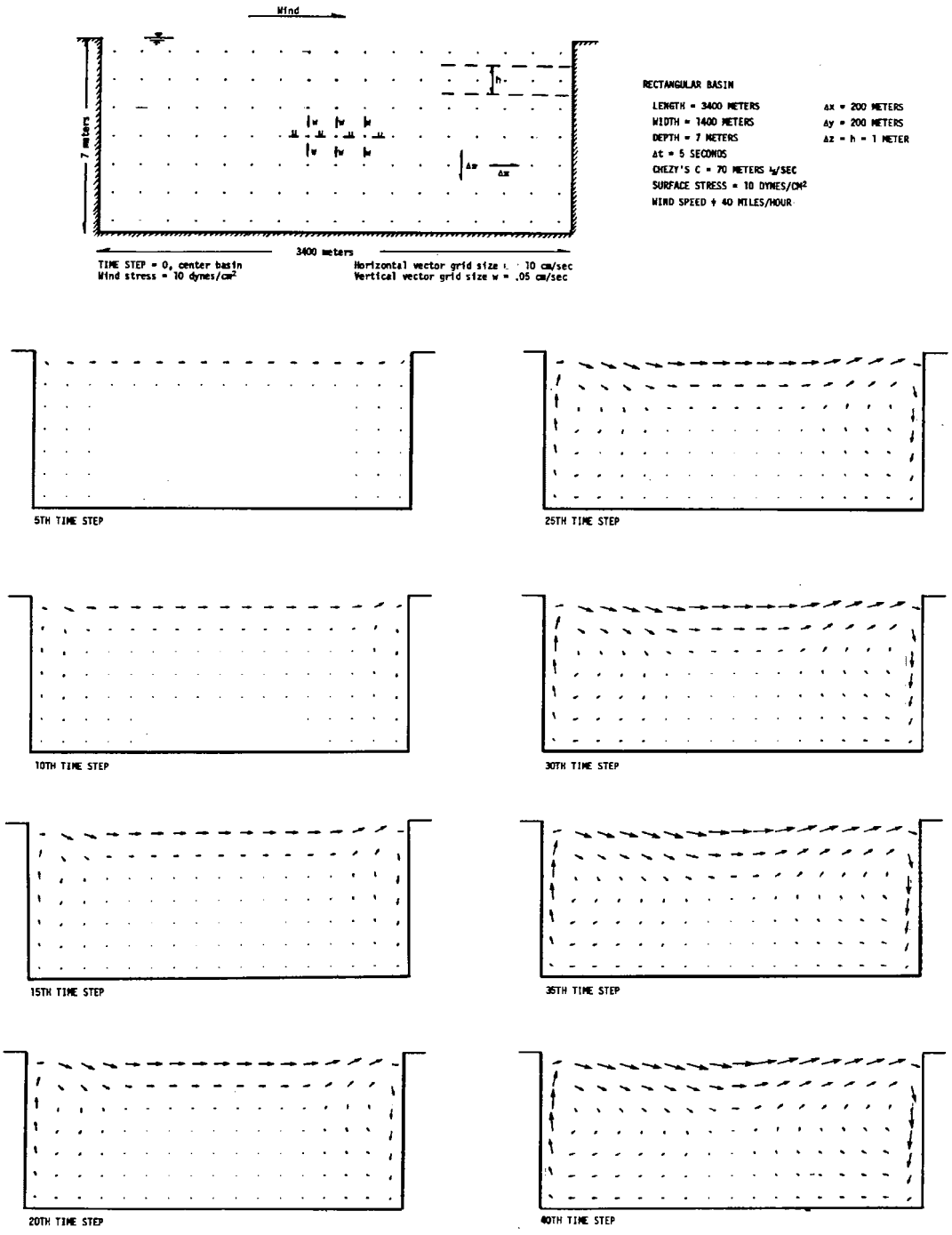

Fig. 6--Transient response of a rectangular basin under easterly wind stress (Part 1)

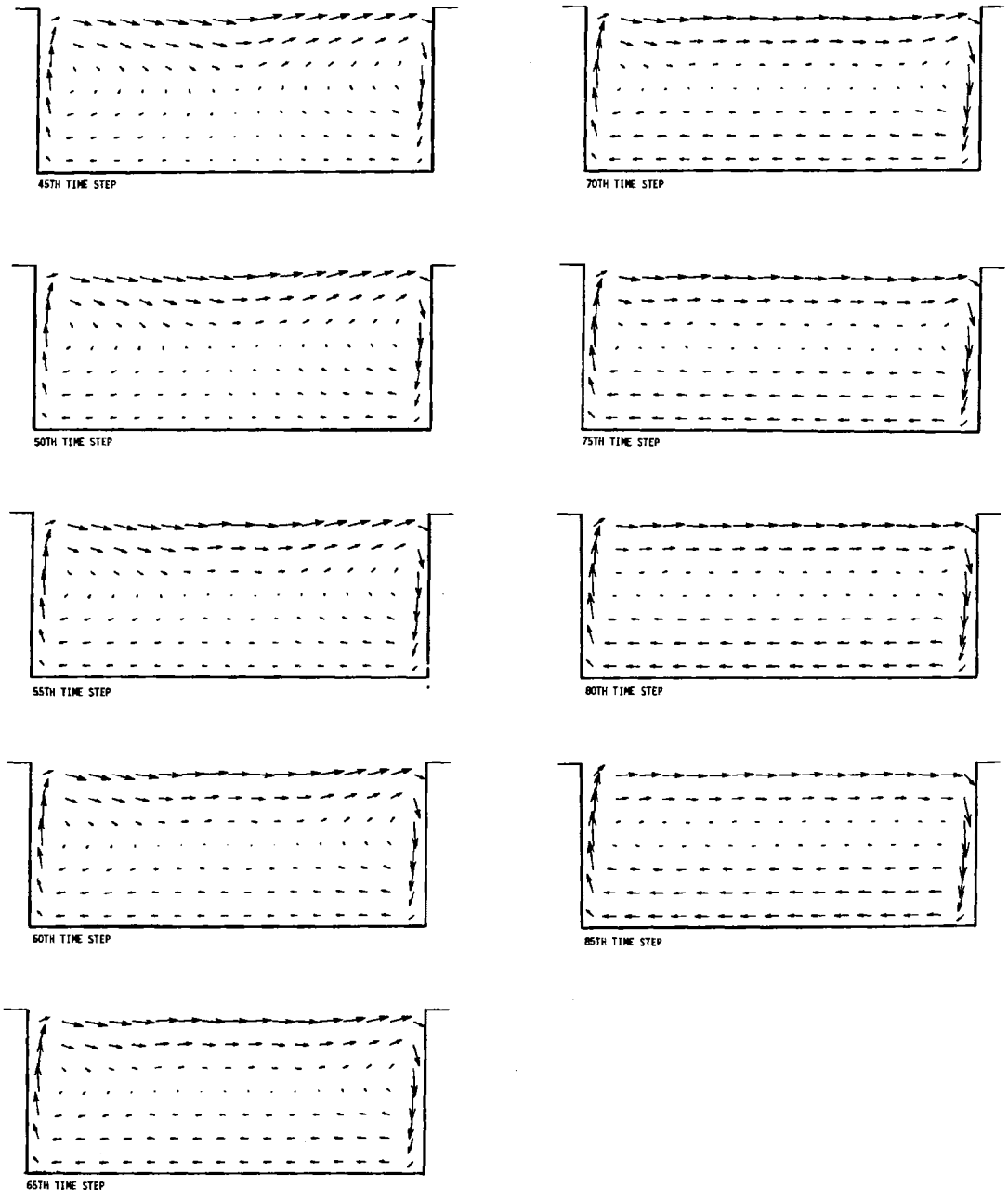

Fig. 7--Transient response of a rectangular basin under easterly wind stress (Part 2)

time steps) show the generation of two large vertical eddies, while the surface current gradually penetrates from the surface layer through the bottom. The next five graphs (45th through 65th time step) show the breaking up of the two elongated eddies and their gradual merger into one large basin-sized eddy in the clockwise direction under the easterly stress. In the last four graphs in this sequence, a layered flow structure is finally established.

Figure 8 shows the development of the vertical velocity profile. In this figure, the u component of different layers at the center point of the basin is plotted. Each profile is identified by a number indicating a 5 time step increment in time. There are fifteen profiles in this sequence, beginning with the water at rest, i.e., the vertical line at the center. As time proceeds, and as the easterly surface current increases, a westerly undercurrent is developed gradually.

Because of the bottom roughness, the current in the bottom layer is retarded, and in turn affects its neighbors by means of viscosity. This interaction continues indefinitely, and the current in the system oscillates around a quasi-equilibrium condition. The velocity profile indicated by arrowheads at each level corresponds to the current map of the 75th time step in Fig. 8. At this time, the profile of the return flow is highly distorted by the bottom friction.

The same physical process can be looked at from a different angle by means of the time histories of velocity at the center basin. Figure 9 shows the time histories of the multi-layered current field at the center section of the basin for the entire simulation period. The duration of the simulation is selected approximately equal to ten times the basic oscillation period of the basin (equal to approximately 164 time steps). In the first few hundred steps the current field becomes established and the basin-wide circulation cell is generated.

As at the beginning of the computation, wind stress suddenly applies energy to the system. Consequently, the basin also starts to oscillate and the velocities belonging to this oscillation are superimposed upon those of the wind-driven circulation. The mean velocities at the top and bottom layer are shown as a dashed line in Fig. 9.

At step 500 the wind stress is removed and the circulation decays. The oscillations of the basin, however, persist.

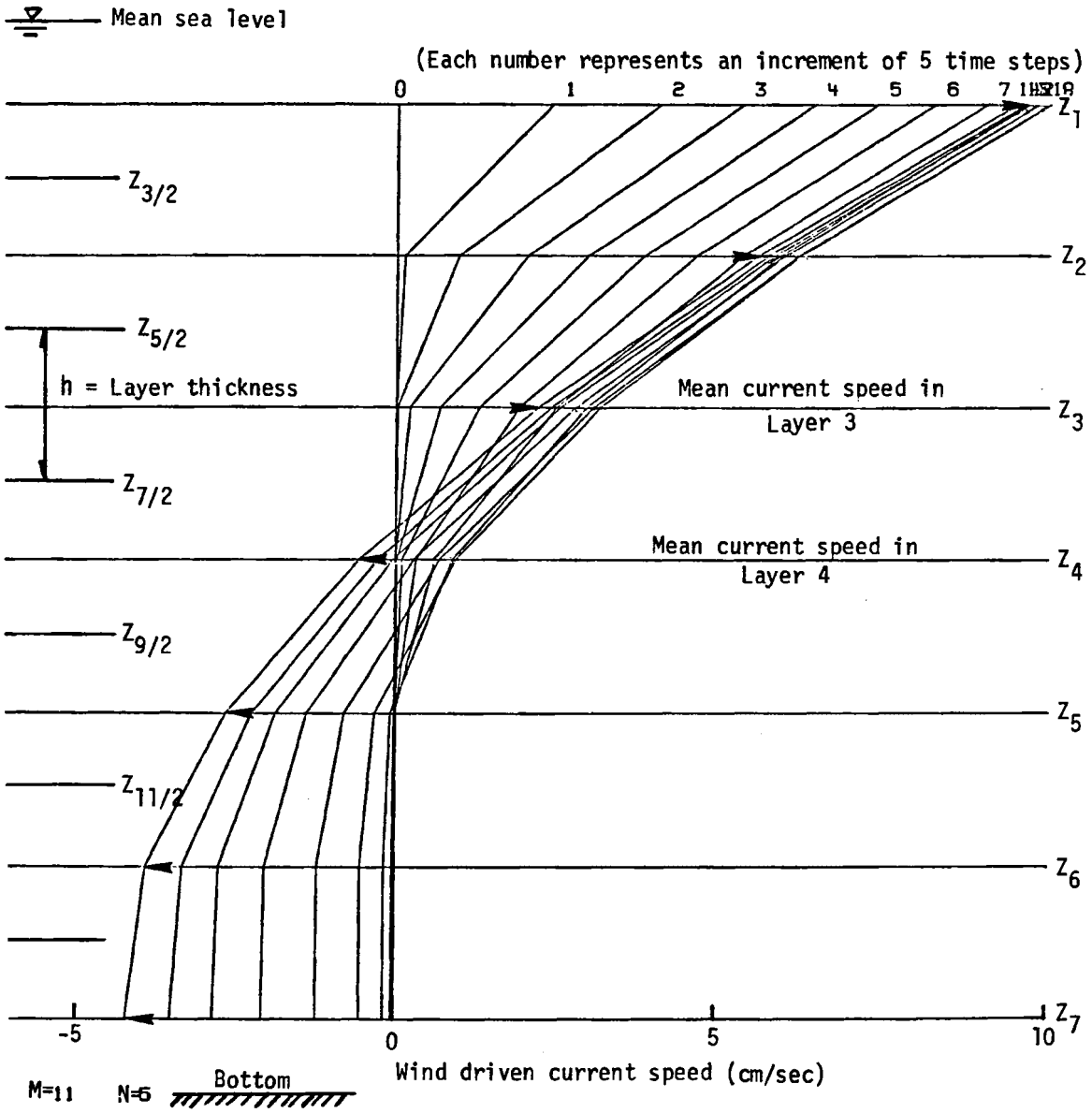

Fig. 8--Initial development of the velocity profile at the center of a rectangular basin under a constant wind stress of 10^{-} dynes/cm^2 (approximate wind speed equals 40 miles/hour)

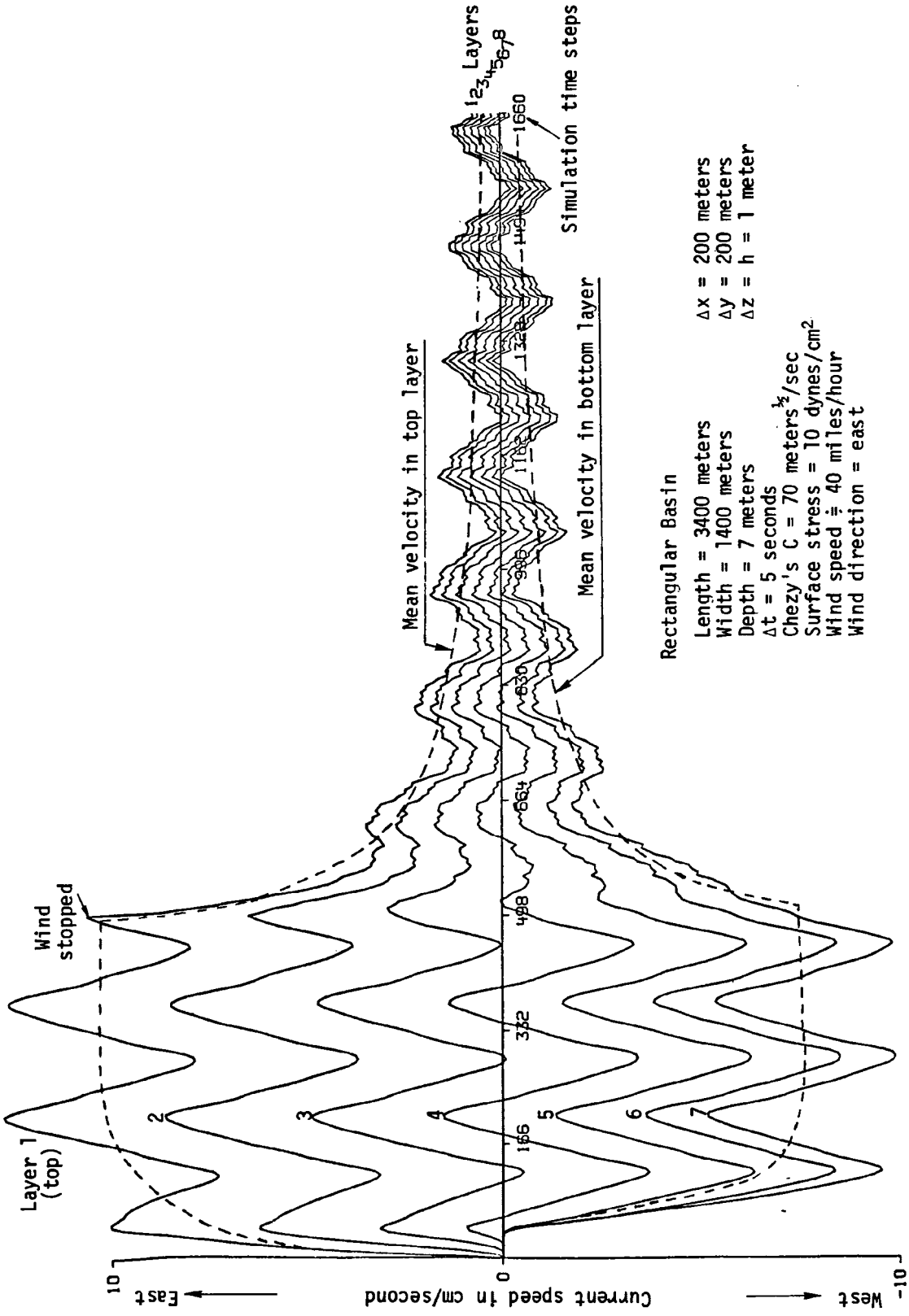

Fig. 9--Time history of the multi-layer wind-driven current speed at the center of a basin

The flow field in the basin is quite complex, as the nonlinearities associated with Navier-Stokes dynamics generate frequency sums and differences. For example, the quadratic stress formulations in the surface, interlayer, and bottom excite principally the odd harmonics of the fundamental frequency. These frequency components are difficult to distinguish from the time histories of variables unless they are mapped onto frequency domain as spectral densities. This analysis will aid development considerably.

Such an analysis was made from time histories of the water level in the center of the basin and the horizontal velocity in the top layer adjacent to it, as no velocity is computed in the center. The computed water level history at that location is shown in Fig. 10, and the computed horizontal current in Fig. 11. The spectral density estimate of the water levels is shown in Fig. 12, and the spectral density estimate of the horizontal current in Fig. 13. The spectral density estimate of the water level shows predominantly even harmonics of the fundamental oscillation frequency of the basin. As for the odd harmonics, the center of the basin is a node. The energy in the records of the water levels decreases with increasing frequency up to .5 cycles per minute. For higher frequencies the energy is about constant. The spectral density estimate of the current shows predominantly odd harmonics. Because the location of the computed currents in this analysis is not exactly in the center of the basin, we do not see the decrease in spectral energy with increasing frequency in such a regular fashion as was the case for the spectral density distribution for the water levels. The estimates of these nonstationary time series were obtained after removal of trends and means in the series.

THREE-DIMENSIONAL WIND-DRIVEN CIRCULATION

In the previous computational test, the wind direction was purposely set eastward to show some important aspects of the basic response characteristics in the x-z plane. In this case, weak secondary circulations do exist due to the Coriolis effect and other nonlinear terms, but they are quite small. In this test series, a diagonal wind stress was imposed on the basin in order to show the characteristics of a three-dimensional

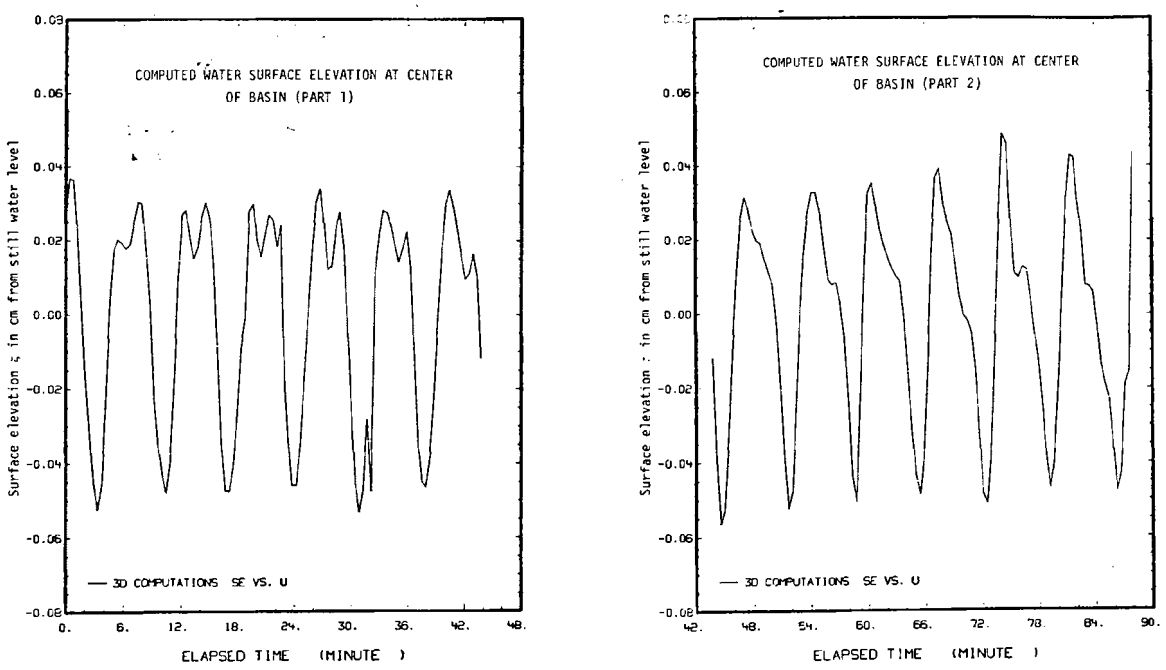

Fig. 10--Computed water surface elevation at center of basin

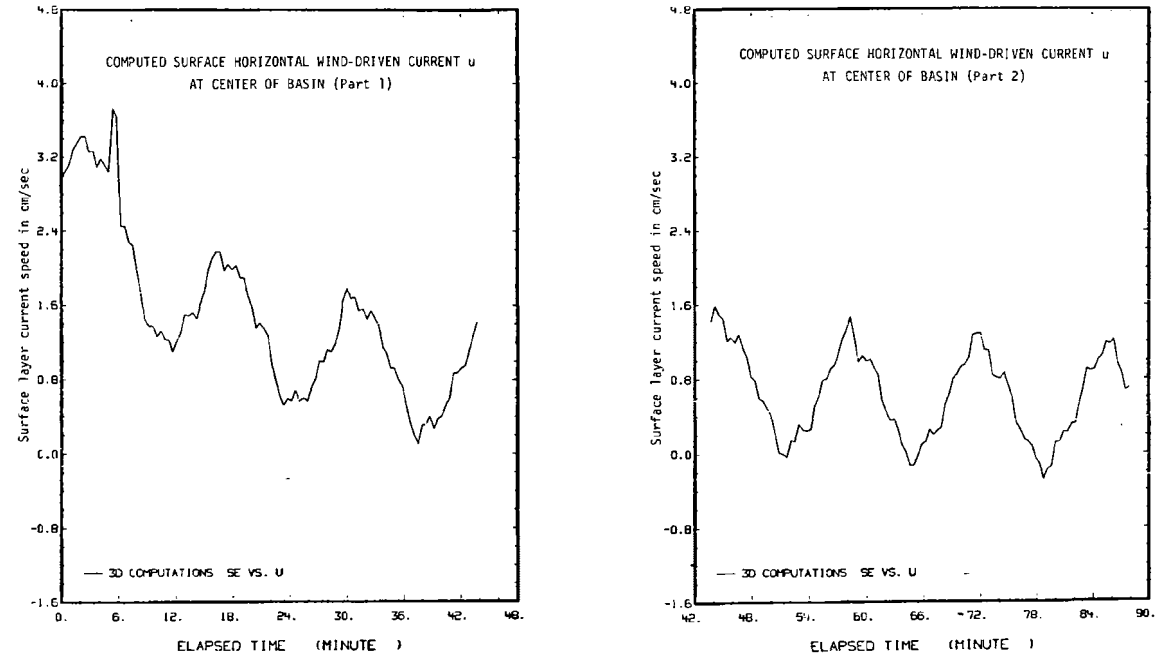

Fig. 11--Computed horizontal wind-driven current at center of basin

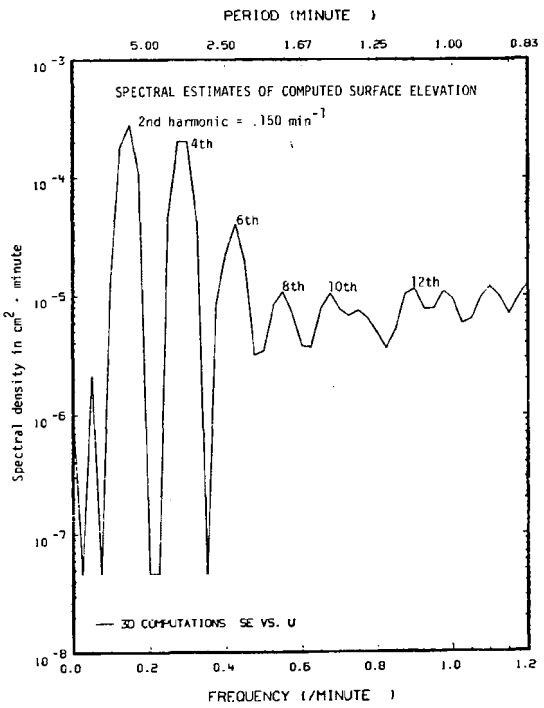

Fig. 12--Spectral estimates of computed surface elevation

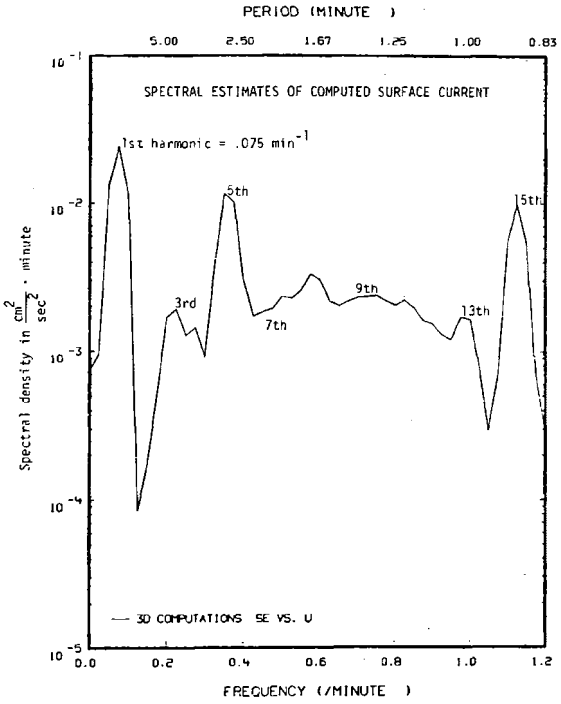

Fig. 13--Spectral estimates of computed surface current

wind-driven circulation. The process of developing the 3-D circulation is extremely interesting, and is illustrated by the series of graphs in Figs. 14 through 18. In this series, only the horizontal velocity vectors at each layer are plotted. In all graphs of this series the velocity vectors have the same scale. If no current exists or if the currents are very small, only a dot will mark the location at which this result was obtained. The gradual establishment of the 3-D circulation can be described by the following sequence:

(1) Initially, current is zero everywhere in the system.

(2) At the 15th time step, a diagonal surface current is established (Figs. 14a and b). Notice the currents at the north and east ends are

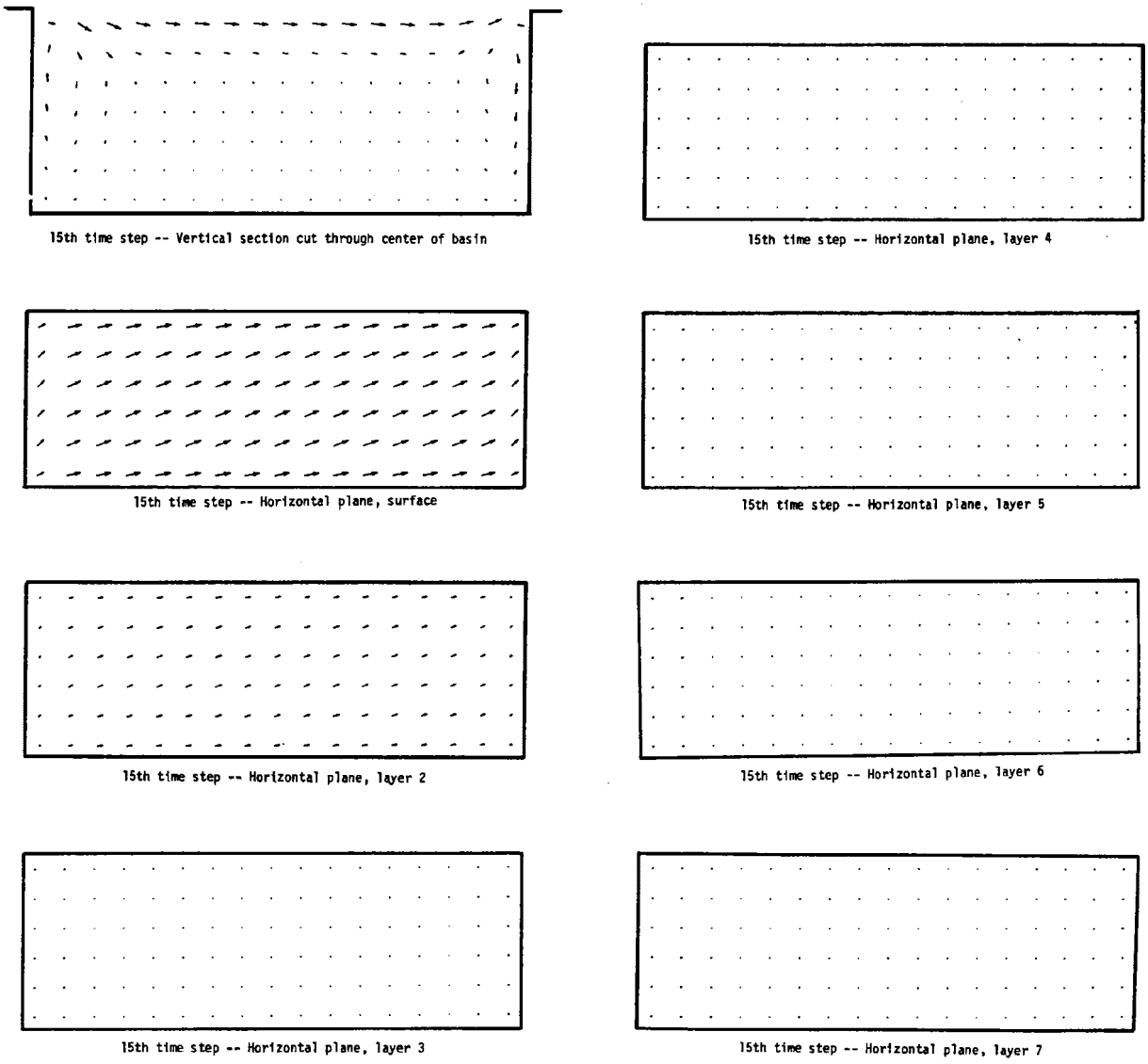

Fig. 14--Velocity components in a cross-section and in seven horizontal layers of a wind-driven rectangular basin at the 15th time step of the computation

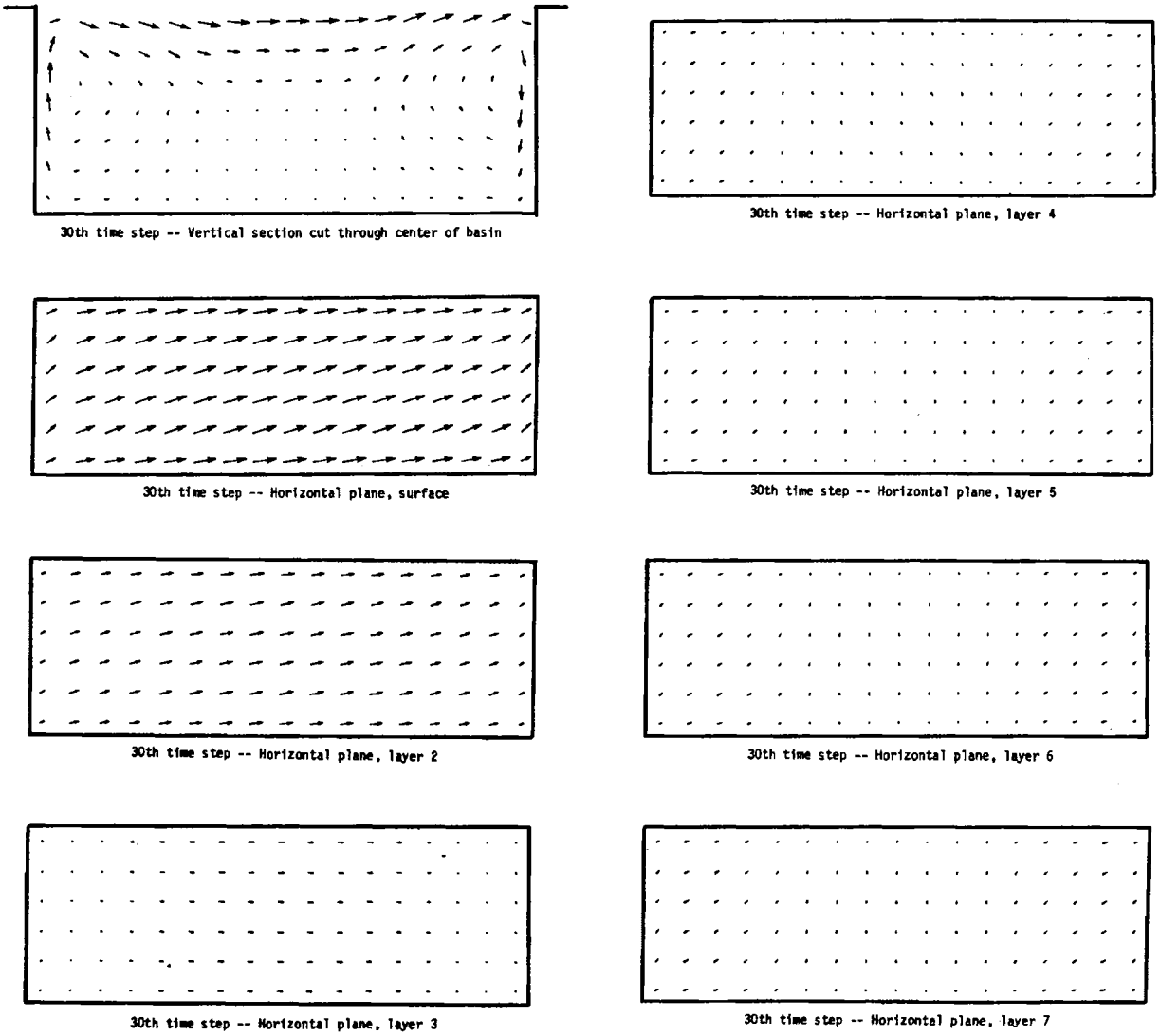

Fig. 15--Velocity components in a cross-section and in seven horizontal layers of a wind-driven rectangular basin at the 30th time step of the computation

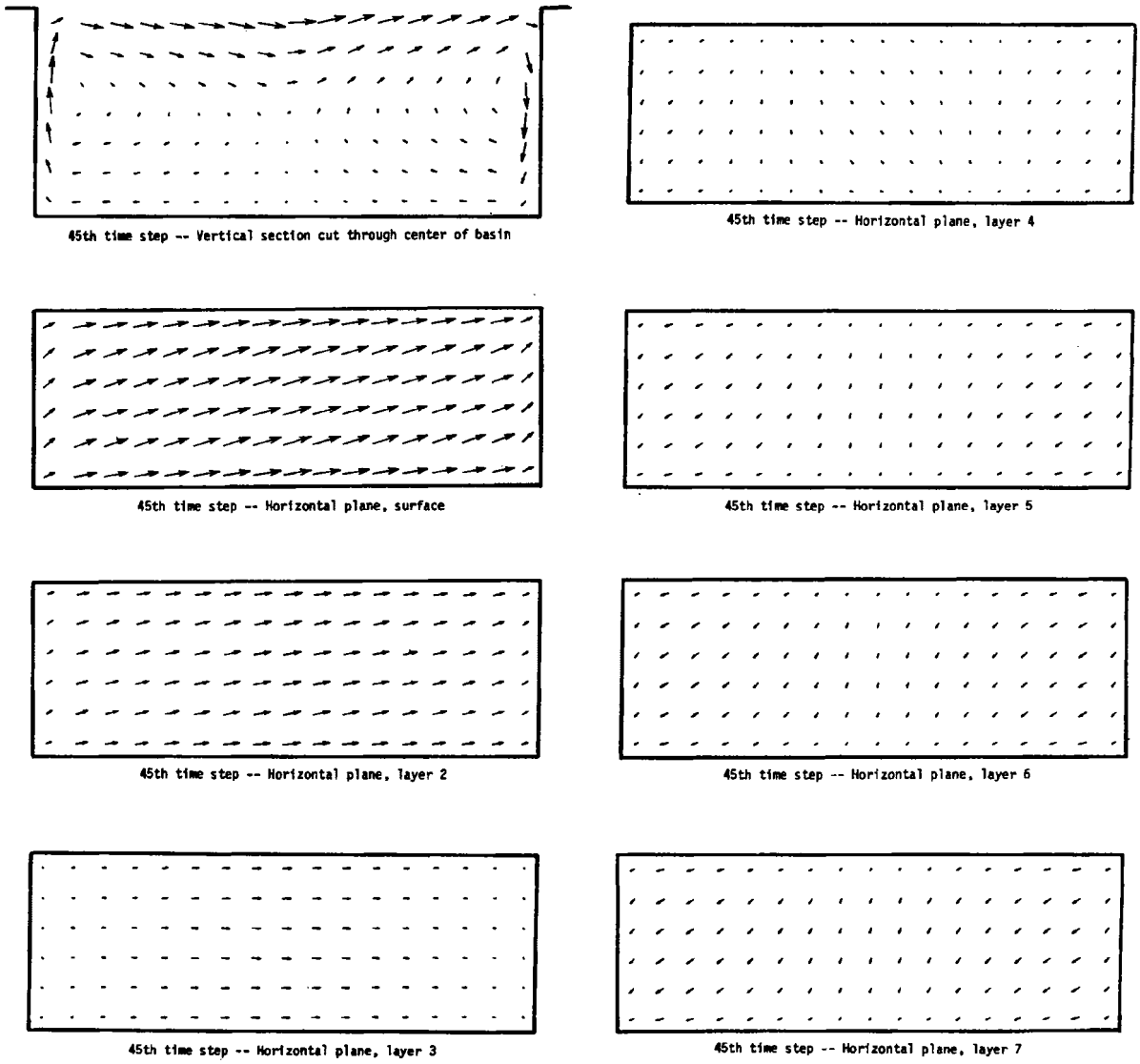

Fig. 16--Velocity components in a cross-section and in seven horizontal layers of a wind-driven rectangular basin at the 45th time step of the computation

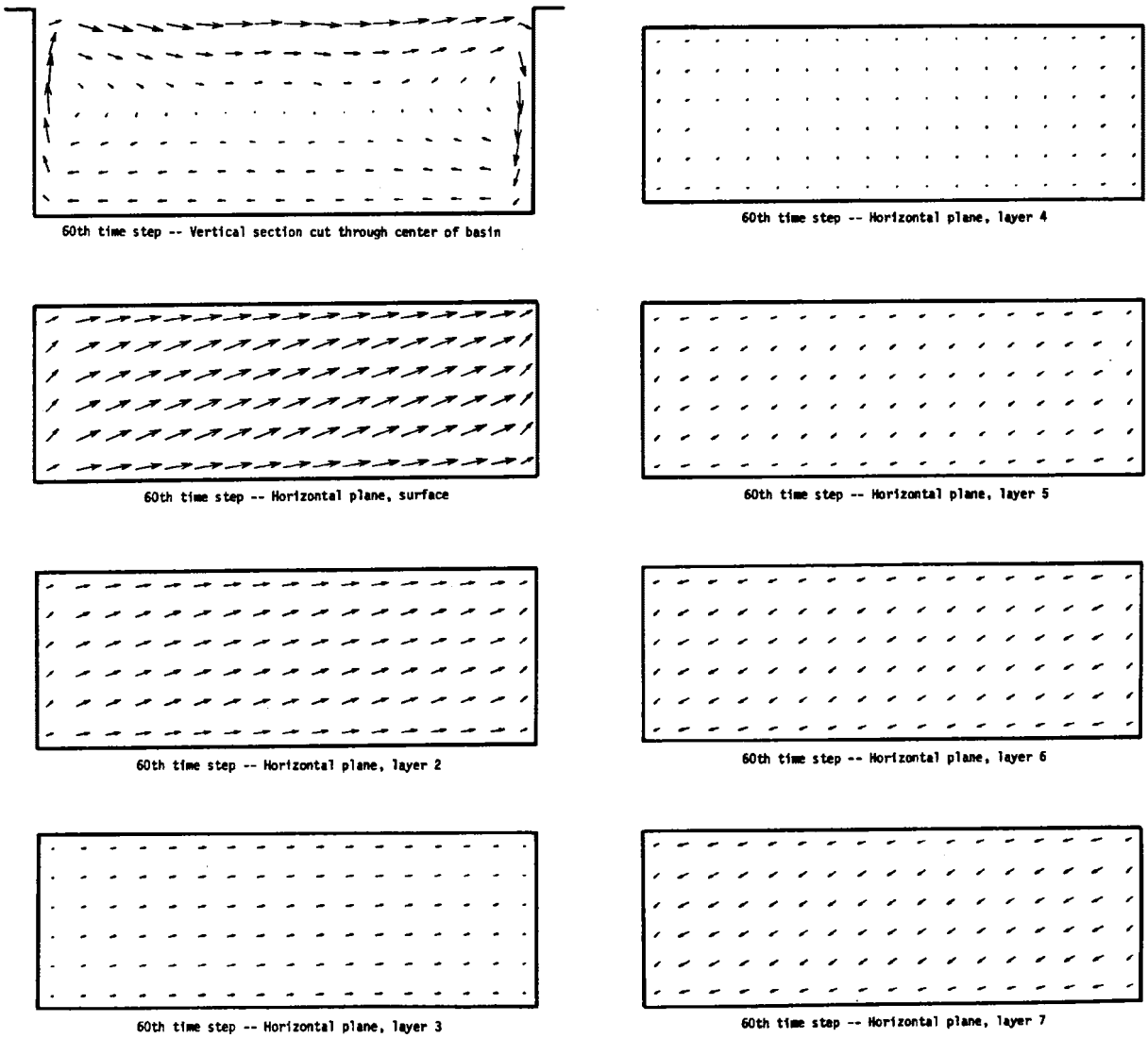

Fig. 17--Velocity components in a cross-section and in seven horizontal layers of a wind-driven rectangular basin at the 60th time step of the computation

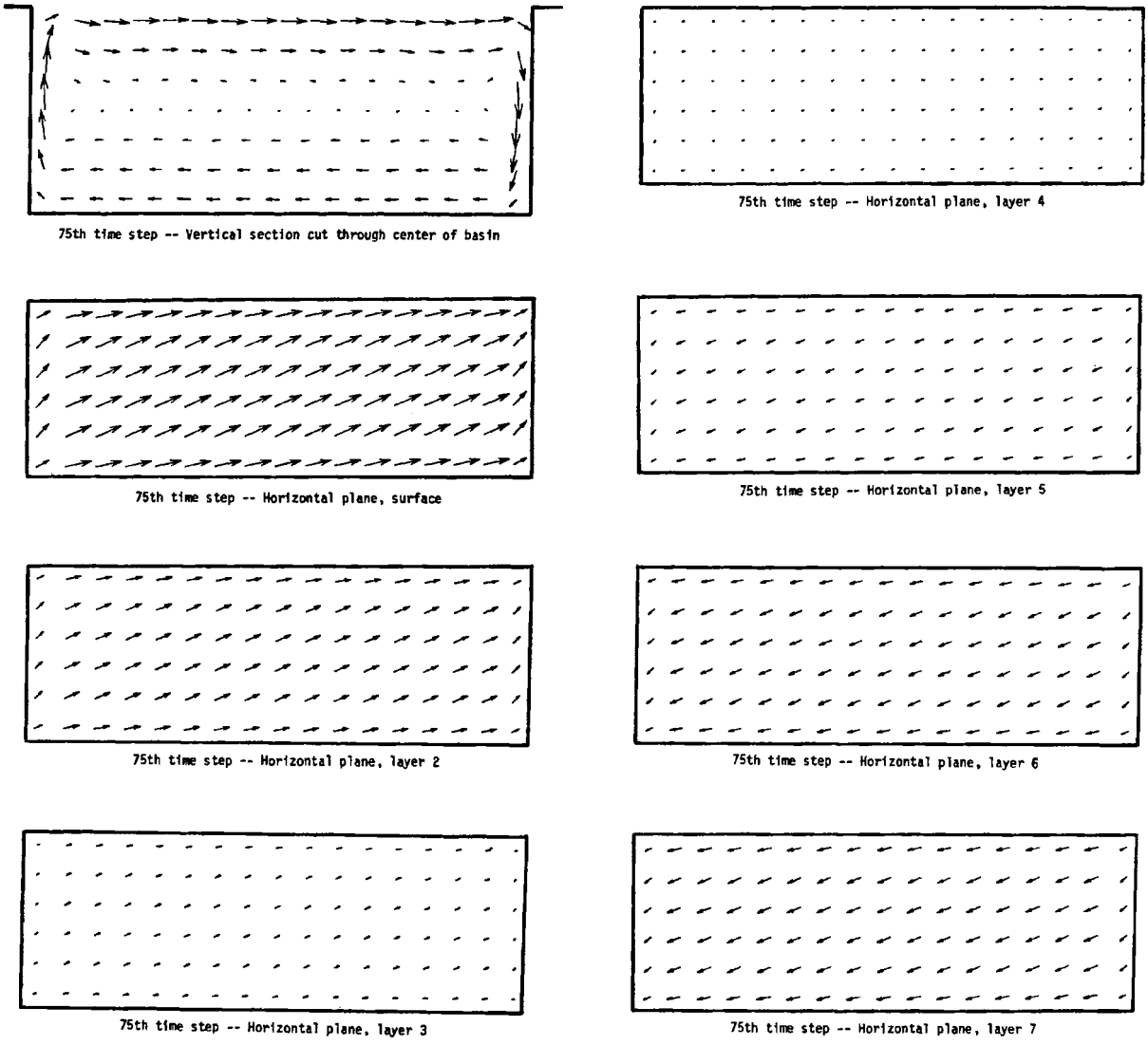

Fig. 18--Velocity components in a cross-section and in seven horizontal layers of a wind-driven rectangular basin at the 75th time step of the computation

deflected due to the kinematic boundary condition. At this time, the vertical velocity component w is pronounced only near the boundaries. The surface drift has already penetrated down to the second layer (Fig. 14c). As indicated by Figs. 14d through 14h, the horizontal velocity components at lower levels are still negligible except near the eastern and western ends where the two local circulation cells are developing.

(3) At the 30th time step (Fig. 15), the wind-driven current has penetrated to the bottom of the basin. The current at the center portion of layer 3 is predominantly horizontal (Fig. 15d) and flows toward the east, whereas the current at both ends is mainly vertical as a part of the growing end-cells. From the graphs of layers 4, 5, 6, and 7 (Figs. 15e, f, g, h), one may notice that two horizontal end-cells are also developed. These two circulation cells are centered around the southeast and the northwest corners. The directions of these two vortices are counterclockwise and clockwise, respectively, where the waters at the center basin are flowing toward the south.

(4) At the 45th time step (Fig. 16), the surface drift current is nearly mature, but the undercurrents are still in their infancies. The direction of current at layer 3 (Fig. 16d) is predominantly longitudinal. The end cells at the southeast and at the northwest are in the elongation process. The currents at the center portion of the basin begin to flow toward south-southwest. Pronounced upwelling and downwelling are now taking place along the southwest and northeast sides, respectively.

(5) At the 60th time step (Fig. 17), the two undercurrent cells are now emerged into one basin-sized loop flowing in a clockwise direction diagonally across the system. A weak secondary circulation still exists. This can be traced in the graph of layer 4, i.e., the midlayer. At this time the countercurrent in the lower layer is not yet fully developed. The delimitation between the top and bottom current is located slightly below the midlayer.

(6) At the 75th time step (Fig. 18), a quasi-steady state circulation is almost established. The effect of bottom friction becomes more pronounced as the undercurrent reaches its maturity. The current

delimitation plane between the surface current and the return current is moved upward due to the bottom current's retardation. At this time, secondary circulations are still in existence, but they are overshadowed by the main circulation in this type of plot.

A PERTURBED DENSITY FIELD

One of the tests in this simulation series involves the computation of wind-driven circulation where a density gradient exists within the system. The initial state was identical to the earlier test, except for a linear vertical salinity gradient that varied from 0 $^{\circ}/_{\circ\circ}$ S at the top layer to 35 $^{\circ}/_{\circ\circ}$ S at the bottom, as shown in Fig. 19, curve A. For this series of computations the temperature was kept constant. Figure 19 shows the transient variation of the wind-disturbed salinity profile at the middle and two ends of a rectangular basin. At the 150th time step, curve B, the salinity profile at the upwind end of the basin shows positive departure from the original one due to the wind-induced upwelling process. Heavier (saltier) water at this locality is originated from the bottom layers mainly through the clockwise circulation process. The salinity departure at the upper layers in the mid-basin is the result mainly of vertical transport and mixing. The positive departure at the top layer in the third graph (downwind end) is caused by the easterly transport. The negative departure at the lower levels is the result mainly of the downwelling process.

At the 300th time step, the same process continues (graph C). If the simulation were carried out indefinitely, the whole basin would be completely mixed by the above-mentioned processes.

SYSTEMS WITH IRREGULAR BOUNDARIES

A series of computational tests were made using water bodies having complex boundary geometries; however, no attempt was made to simulate a real event using observed field data. The computations were conducted for testing the scheme.

The bathymetry and shape of Lake Michigan was selected for the test. The system consisted of a horizontal grid structure of 48 × 20 with grid size being 11.7 kilometers. The model has eight layers. Each layer is 30 meters deep. The system's density structure was assumed to be uniform.

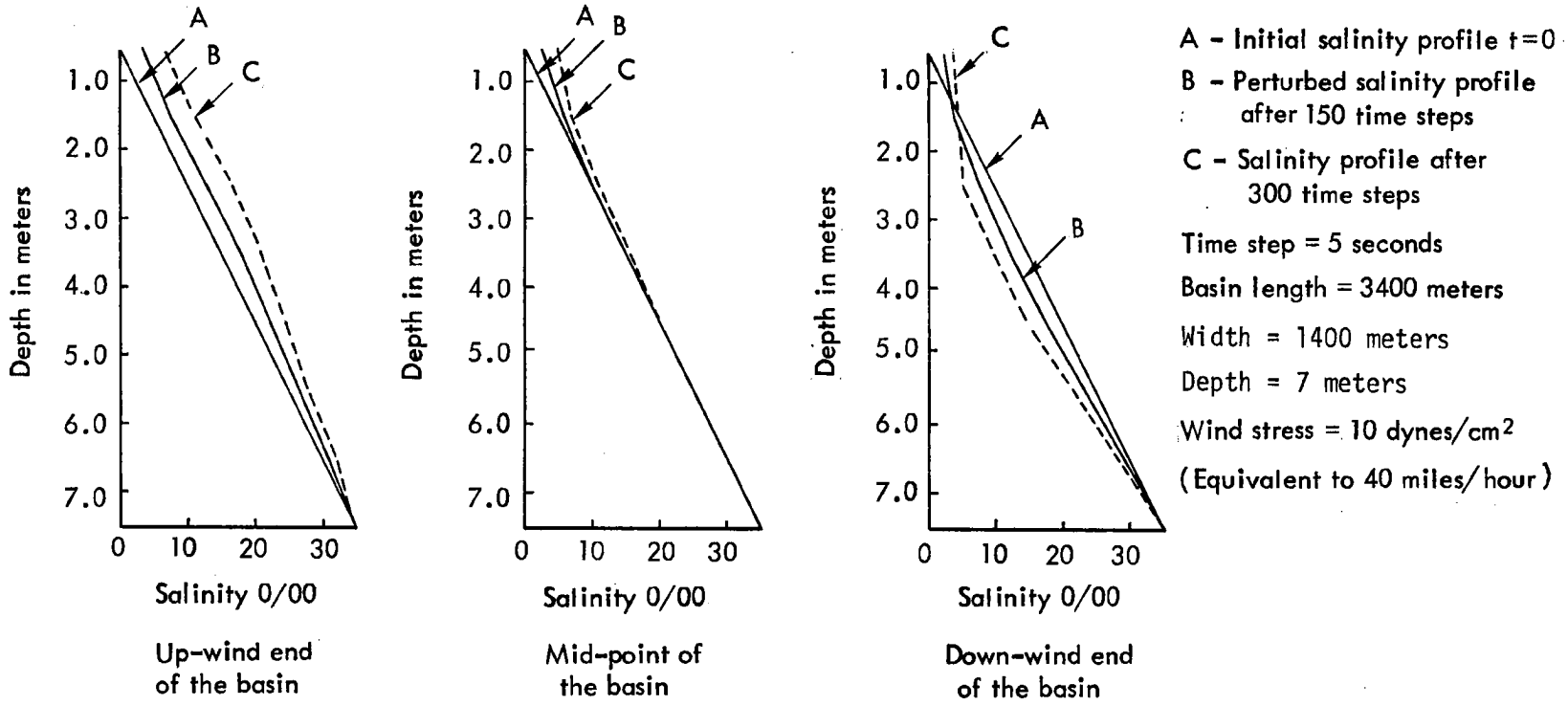

Fig. 19 — Transient variation of salinity profile for a simple testing case. Rectangular basin under constant wind stress.

A constant wind stress of 0.5 dynes/cm^2 (equivalent wind speed $\approx$ 9 miles/hr) was imposed uniformly upon the surface from the south. The lake was at rest in the beginning. The computation was carried out up to 4000 integration time steps with Δt equal to one minute in real time.

After 500 minutes (Fig. 20a), the surface drift current is predominantly to the right due to the Coriolis effect, except near the boundaries, where a belt of long-shore drift is most pronounced. A clockwise eddy is beginning to form at the south end of the lake, whereas a counterclockwise circulation is evident near the northeastern corner.

At depths between 30 and 60 meters (Fig. 20b), the horizontal movements of water are characterized by the returning current at the shallower areas. Near the deeper regions, the drift currents deflected further to the right (southeasterly flow) with reductions in speed. At areas of intermediate depths, the boundary effect interacts with the Coriolis effect, forming complicated circulation patterns. Long-shore movements still exist near the straight western shore.

At depths between 60 and 90 meters (Fig. 20c), the long-shore movements in the direction of the wind no longer exist, with the exception of the return current. The predominant horizontal currents tend to follow the bottom contours of the system. In layer 4 (Fig. 20d), the general current pattern is approximately the same as level 3, except the current direction in the deeper areas deflects farther to the right (southwesterly flow), implying that the Coriolis effects still overshadow the boundary effects. The predominant currents in the deeper basins of the lake (Fig. 21) are induced mainly by the pressure gradient created by wind stress. In this sequence of diagrams the scale of the velocity vectors is 3 cm/sec to a grid size.

In the next sequence (Figs. 22 and 23), a velocity scale of 5 cm/sec to a grid size is used. This set of maps shows the circulation pattern after 4000 minutes (67 hours). In the surface layer (Fig. 22a), the stronger currents are along the shore, forming belts approximately 15 kilometers wide. The strongest cross-lake (east-west) currents are located at areas where the depths are deepest, namely, the south and north basins. In the shallower portion of the south end, a clockwise circulation is formed, whereas a counterclockwise eddy exists at the northeastern corner of the lake.

At depths between 30 and 60 meters (Fig. 22b), the only long-shore

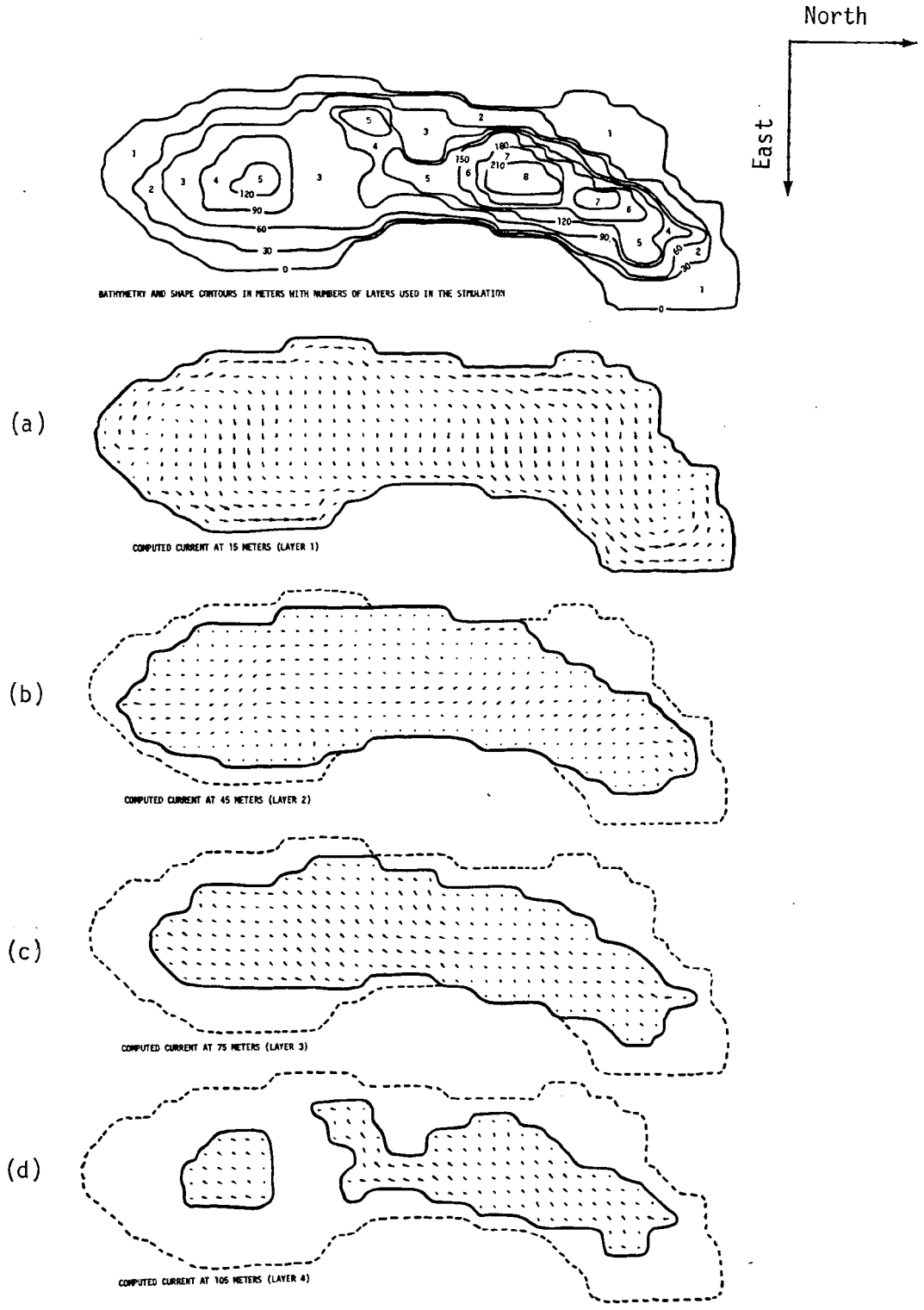

Fig. 20--Velocity components in the four upper layers of a wind-driven homogeneous lake with irregular boundaries at the 500th time step (see text)

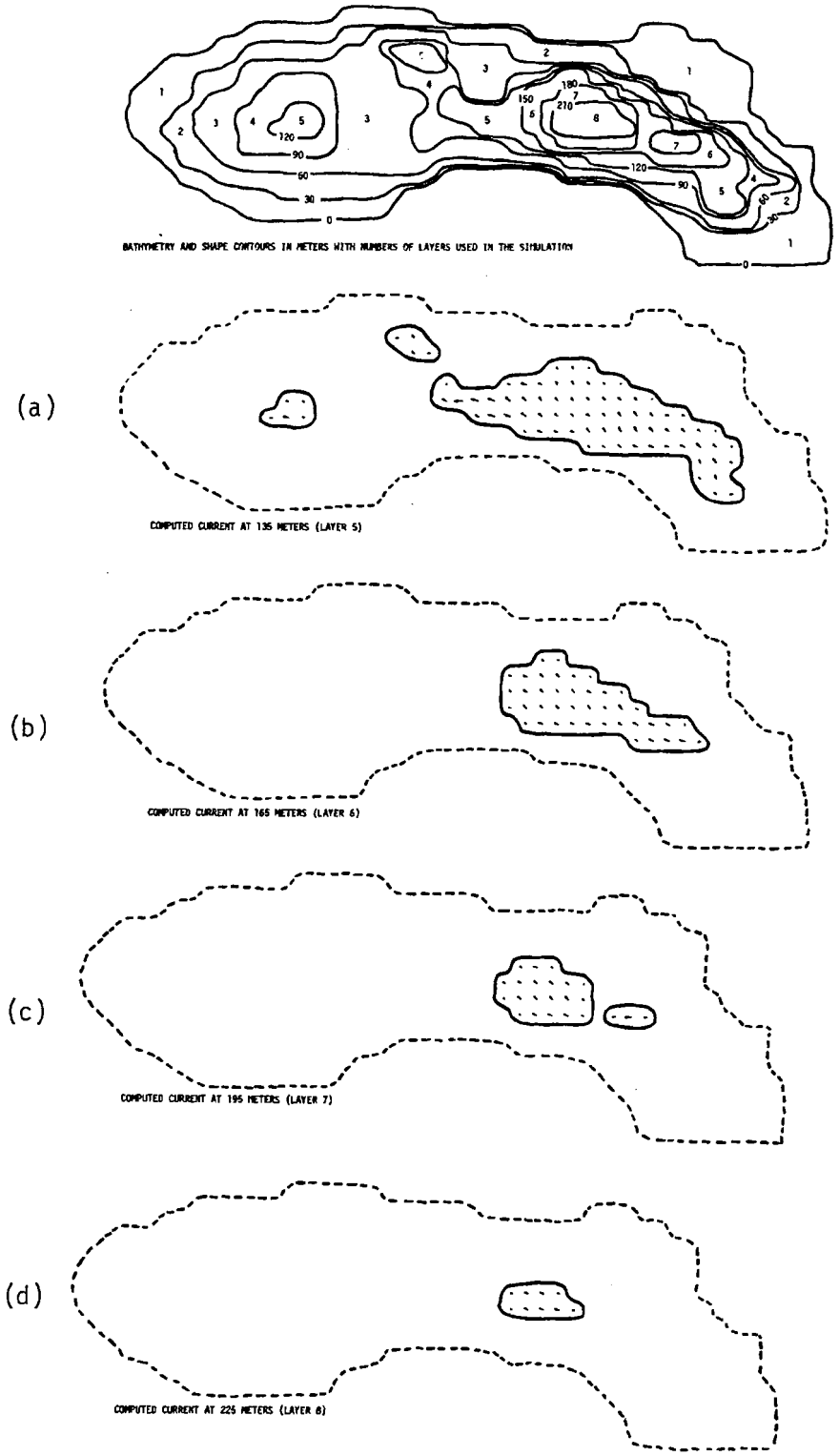

Fig. 21--Velocity components in the four lower layers of a wind-driven homogeneous lake with irregular boundaries at the 500th time step (see text)

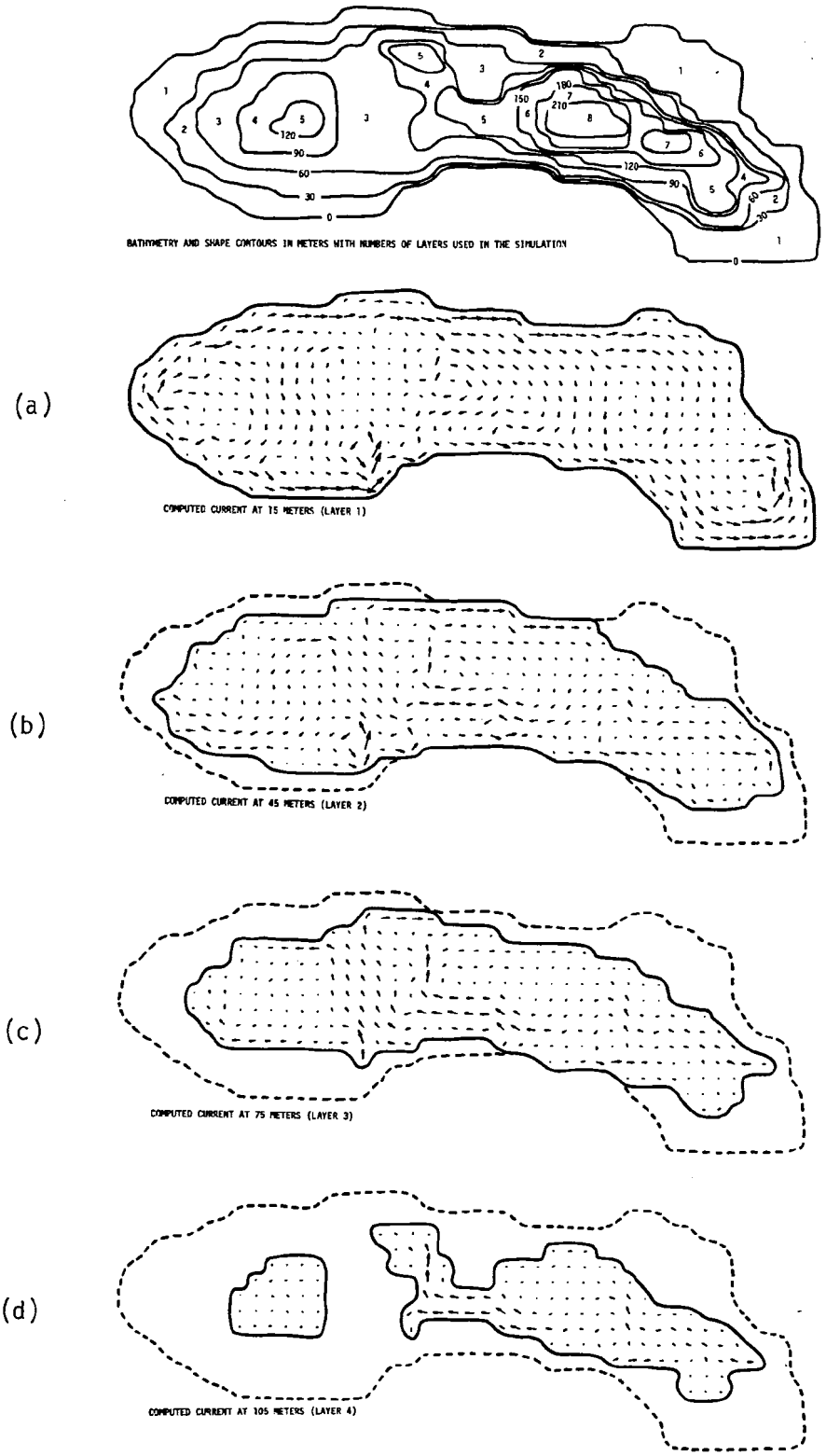

Fig. 22--Velocity components in the four upper layers of a wind-driven homogeneous lake with irregular boundaries at the 4000th time step (see text)

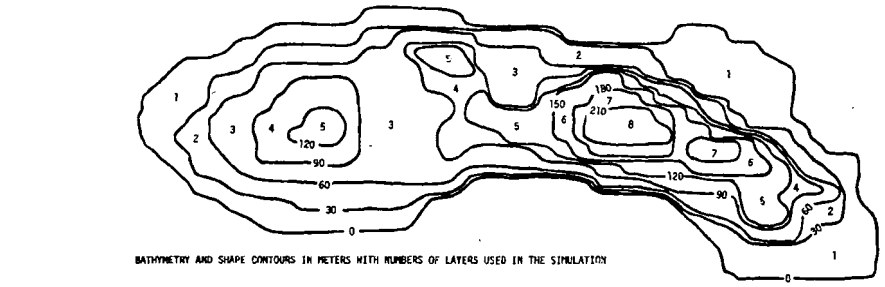

(a)

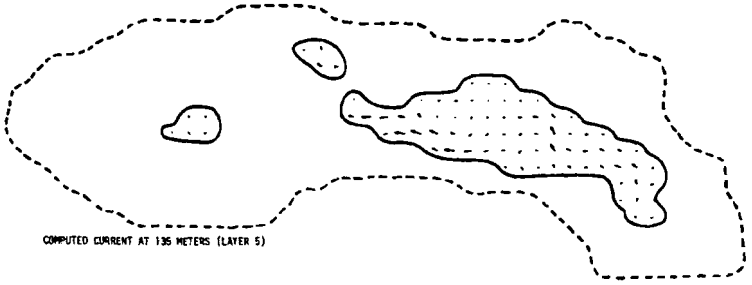

(b)

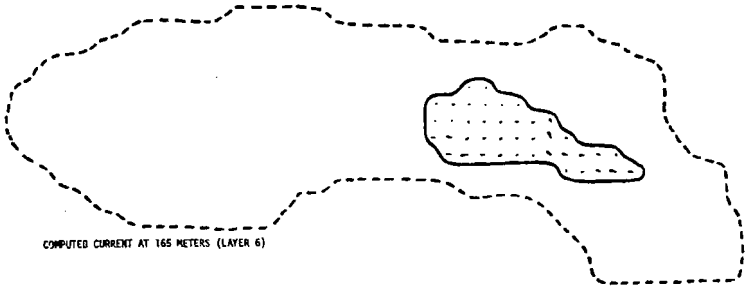

(c)

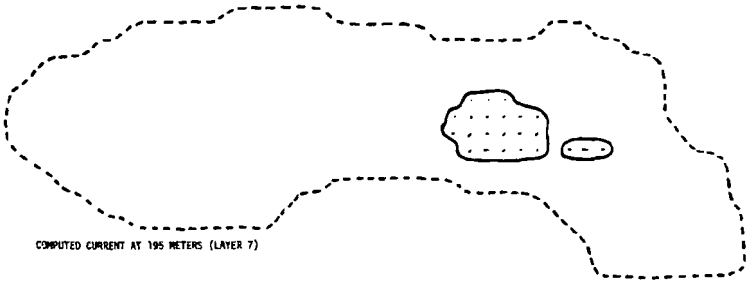

(d)

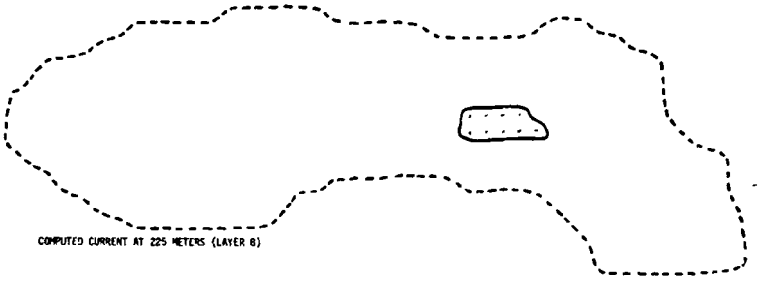

Fig. 23--Velocity components in the four lower layers of a wind-driven homogeneous lake with irregular boundaries at the 4000th time step (see text)

component is located near the straight stretches of the western shore.

The stronger return currents are located near the deeper north basin. The strongest horizontal movement of water is the westward subcurrent, which rushes through the shallower portion between the two basins. This current then branches into two long-shore components flowing in opposite directions along the western bank.

In layer 3 (Fig. 22c), two counterclockwise eddies are located at two ends, while a return current flows meanderingly in the middle of the north basin. In the fourth layer of the south basin (Fig. 22d), the magnitude of the currents is extremely small, but, on the other hand, significant current components still exist in the north basin; these currents are induced by the surface gradient set up by the wind stress. In the lower layers all the currents are small (Fig. 23).

Figure 24 shows the gradual establishment of the wind-driven current at a particular location. It can be seen that after 3000 minutes from the beginning, the current field is almost steady state. Oscillations during the earlier stage coincide with the seiche mode of the lake, which is approximately 8 hours. The inertial period for the lake is approximately 17.4 hours at latitude 45°N.

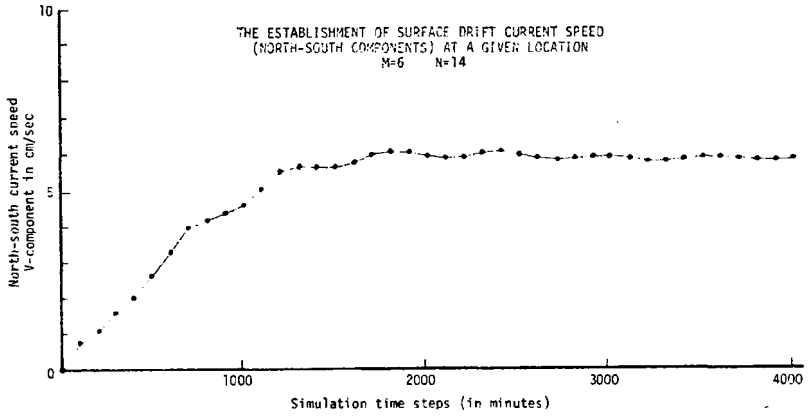

Fig. 24--The establishment of drift current speed at a given location

V. DISCUSSION

As indicated in the description of the physical processes, an approximation has been made by assuming that the pressures are hydrostatic. This approximation would preclude the application of the model to cases with very nonuniform flow where the vertical accelerations are not negligible. In the application of the model to estuaries, however, this assumption is well justified.

The assumption of hydrostatic pressure distributions has a very pronounced effect on the computability of the flow. If vertical accelerations are also incorporated in the formulation, the three momentum equations have to be solved simultaneously with the continuity equation, which would increase the computational effort considerably.

The formulation of the dispersive transports in the momentum equations and the mass transport equations for the model follows a conventional Fickian approach. These coefficients can, at a later time, be made dependent on some of the local properties of flow field and density field.

In the vertical momentum exchange, quadratic terms have been introduced; this can be extended by an additional exchange term that relates the momentum exchange linearly to the horizontal velocity gradient. Such an extension would make the model somewhat more flexible in adjustment; particularly as in modeling of ocean circulation, such an approximation is used and exchange coefficients have become available from experiments.

In the finite difference scheme, an approximation of the momentum equation is used in which the momentum is expressed as the product of layer thickness and the velocity component. Several other choices did exist—for example, an operation upon the momentum U, where U represents the momentum, or a computation according to the semimomentum method, thus using only operations on the velocity components.

The latter method would result in less complicated expressions for the momentum equations, but considerable difficulty would be encountered in expressing the top and bottom layers, with their variable thicknesses, in a manner such that the scheme would conserve quadratic properties of

physical significance such as kinetic energy for the horizontal flows.

Use of the operation on the momentum expressed as variables U, V also precludes conservation of a quadratic property--in this case, the kinetic energy. This has been shown for a two-dimensional model by Leendertse.[10]

Two basic methods of integration are suitable for solving difference equations of this type. It is required that wave motions do not decay in time by the method; thus, the computation scheme should not have dissipative properties. The schemes that could be used are the previously discussed leap-frog method, or an alternating direction implicit method. A completely implicit method is not feasible, as extremely large matrices have to be solved, which is very time-consuming. The alternating direction implicit method such as the one used for two-dimensional computation could be applied, as it is fast and can use larger time steps than the leap-frog method.

Considerable experience has been obtained with the alternating direction implicit method, but this integration method was not selected for two reasons. First, the alternating direction integration method requires that all computational arrays be in the computer's fast memory unit for efficient computation. This may put considerable restraint on the array sizes of the model. The explicit method can use all array information in a certain sequence, thus it would be possible to have only part of large computational arrays in the fast memory unit, while simultaneously data is transferred in and out of this fast memory unit. Such a process is not feasible for the alternating direction method.

Secondly, the alternating direction solution was not used as it would place restrictions on formulating the finite difference scheme, which could affect conservation of quadratic properties. In the alternating direction method, three unknown values exist for each equation. For the continuity equation, two momentum values are unknown, together with one pressure value, while in the equation of motion, one momentum value is unknown and two pressure values. As these systems of equations for each row or column of the horizontal arrays are solved by recursions, the pressure values and the momentum values should be of the same magnitude. If this is not the case, the method will be inaccurate because of the truncations. As with the two-dimensional model, velocities and pressure in the form of water levels could be used, but this would have less favorable conservation properties, as mentioned above.

A leap-frog scheme has a limit on the size of the time step; exceeding this limit makes the computation unstable. According to Grammeltvedt,[11] the maximum time step for a system, if the Coriolis terms and advection terms are neglected, is

$$\Delta t_{max} = \Delta x \sqrt{2gh_{max}}$$

where h_{max} = maximum depth in the system.

The alternating direction implicit method has no stability condition; the maximum time step is controlled by the required accuracy of the computation. Leendertse[12] has shown that the propagation of long waves becomes affected if the time step exceeds 3 to 5 times the limit defined in Eq. (71).

The leap-frog scheme was adopted, as the disadvantage of a smaller time step was considered less severe than the limitations imposed by the use of an alternating direction method. Although the computations with the adopted scheme are extensive, the method is still well within the range of practical application. For example, the simulation of the lake, described in the previous chapter, with a horizontal grid of about 1000 points and with eight layers, required a computation time of 30 minutes on an IBM 360-91 for a real time simulation of 67 hours in 4000 time steps. In this simulation the salinity was also computed, even though a constant initial value was assumed.

Lilly[13] analyzed the expression for the horizontal advection used in the scheme, and he shows that for the horizontal motions the energy in the computation is maintained except for sources from wind and sinks by turbulent diffusions. A rigorous analysis of the approximations for the vertical advective transports has not yet been accomplished; this analysis was not included in the scope of this investigation.

From the numerical experiments some evidence exists that the formulation is close to conservation of energy, or does conserve energy, otherwise the computation of the oscillating basin without energy dissipation would have become unstable, or the motions would have decayed.

In the formulation we have emphasized conservation of physical quantities. The aspects of energy conservation have already been

mentioned. It may also be possible to conserve enstrophy, which can be defined as half the squared vorticity, as indicated by Arakawa.[14] A further extension of the model development should investigate whether such an extension would be advantageous. The expressions for the advection become very complicated if conservation of enstrophy is to be achieved. This will increase the computational effort, and also may make the boundary descriptions very complex.

Conservation of mass is achieved in the computation, as can be seen directly from the finite differences. Summation of the terms on the right-hand side of Eq. (56) over the whole computational field equals zero if all boundary fluxes are zero; thus in the computation no water is added by the computation procedure used. This is also the case for the advective transport equation of salt (Eq. 59).

In simulating the lake, the bottom of the lake was approximated in steps of the layer thickness. The approximation of the bottom in this manner is far from satisfactory, as the discrete changes in vertical direction are introduced which can result in deformations of the flow field in the vicinity. As the layer thickness is included in the computation, the bottom layer can be varied in a manner similar to two-dimensional models with vertically integrated flow. It is expected, however, that a considerable program development would be required to accomplish this.

From the few sample computations presented in this report, it is clear that graphical representation of results is the major method by which computation results can be analyzed. In the report only currents have been represented in horizontal and vertical planes. An effective use of the model also requires representation of the salinity distributions, the energy, and the vorticity, to mention a few. An exploration of appropriate methods for representing results would be one of the next major steps to undertake in the continued development. Experience has shown that even with such powerful graphics as IGS, the major time delay occurs in processing computed data.

In this report, only salinity was considered to influence the pressures in the fluid. But temperature also influences the pressures, thus the formulation should be extended to incorporate the transport of

heat. In that case the range of applications of the model would be extended also, as in many inland water bodies the temperature, together with wind, are the main driving forces of the fluid motions.

VI. CONCLUSIONS AND RECOMMENDATIONS

The three-dimensional flows in estuaries and other large water bodies with nonisotropic density distributions can be computed according to the principles of computation developed in this report. To make the program directly applicable to engineering investigations, the following studies and developments must be made:

(1) Formulate and develop the computational code for boundaries, such as those that occur at the bottom, sides, and the seaward ends of the model, based upon realistic formulations of the local physical processes and conditions.

(2) Investigate the transfer of energy from one frequency range to another in the model by analyzing properties of the finite difference scheme and by experimenting with different formulations of the advective terms in the equations of motion.

(3) Develop methods for graphically representing results.

(4) Incorporate the transport of heat in the model, together with the interaction of temperature distributions with the fluid flow.

Appendix
EXPANSION OF A MOMENTUM EQUATION

The computational code was directly derived from the finite difference equations in the compact form as used in this report. For the reader who is not yet experienced in reading finite difference equations in the manner presented in this report, the terms of the horizontal momentum equation in x-direction are presented with an expanded form, with the variables identified by indices. The equation is determined on the point $(i + \frac{1}{2})\Delta x, j\Delta y, k\Delta z, n\Delta t$. The terms are as follows:

$$\overline{\delta_t(\overline{h}^x u)}^t = \frac{1}{4\Delta t}\left\{\left(h_{i,j,k,n+1} + h_{i+1,j,k,n+1}\right) u_{i+\frac{1}{2},j,k,n+1} - \left(h_{i,j,k,n-1} + h_{i+1,j,k,n-1}\right) u_{i+\frac{1}{2},j,k,n-1}\right\} \tag{A-1}$$

$$\begin{aligned}\delta_x\left(\overline{\overline{h}^x u \overline{u}^x}^x\right) = \frac{1}{8\Delta x}\Bigg[&\left\{\left(h_{i+1,j,k,n} + h_{i+2,j,k,n}\right) u_{i+3/2,j,k,n} + \left(h_{i,j,k,n} + h_{i+1,j,k,n}\right) u_{i+\frac{1}{2},j,k,n}\right\}\left(u_{i+3/2,j,k,n} + u_{i+\frac{1}{2},j,k,n}\right)\\ &- \left\{\left(h_{i,j,k,n} + h_{i+1,j,k,n}\right) u_{i+\frac{1}{2},j,k,n} + \left(h_{i-1,j,k,n} + h_{i,j,k,n}\right) u_{i-\frac{1}{2},j,k,n}\right\}\left(u_{i+\frac{1}{2},j,k,n} + u_{i-\frac{1}{2},j,k,n}\right)\Bigg]\end{aligned} \tag{A-2}$$

$$\delta_y\left(\overline{\overline{h^y}^x v \overline{u^y}}\right) = \frac{1}{8\Delta y}\left[\left\{\left(h_{i+1,j+1,k,n} + h_{i+1,j,k,n}\right) v_{i+1,j+\frac{1}{2},k,n}\right.\right.$$
$$\left.+ \left(h_{i,j+1,k,n} + h_{i,j,k,n}\right) v_{i,j+\frac{1}{2},k,n}\right\}\left(u_{i+\frac{1}{2},j+1,k,n} + u_{i+\frac{1}{2},j,k,n}\right)$$
$$- \left\{\left(h_{i+1,j,k,n} + h_{i+1,j-1,k,n}\right) v_{i+1,j-\frac{1}{2},k,n}\right.$$
$$\left.\left.+ \left(h_{i,j,k,n} + h_{i,j-1,k,n}\right) v_{i,j-\frac{1}{2},k,n}\right\}\left(u_{i+\frac{1}{2},j,k,n} + u_{i+\frac{1}{2},j-1,k,n}\right)\right] \tag{A-3}$$

$$\overline{h^x}\delta_z\left(\overline{u^z w^x}\right) = \tfrac{1}{4}\left[\left(u_{i+\frac{1}{2},j,k-1,n} + u_{i+\frac{1}{2},j,k,n}\right)\left(w_{i+1,j,k-\frac{1}{2},n} + w_{i,j,k-\frac{1}{2},n}\right)\right.$$
$$\left.- \left(u_{i+\frac{1}{2},j,k,n} + u_{i+\frac{1}{2},j,k+1,n}\right)\left(w_{i+1,j,k+\frac{1}{2},n} + w_{i,j,k+\frac{1}{2},n}\right)\right] \tag{A-4}$$

$$f\ \overline{h^x}^{xy} = \frac{1}{8} f\left(h_{i+1,j,k,n} + h_{i,j,k,n}\right)$$
$$\left(v_{i+1,j+\frac{1}{2},k,n} + v_{i,j+\frac{1}{2},k,n} + v_{i+1,j-\frac{1}{2},k,n} + v_{i,j-\frac{1}{2},k,n}\right) \tag{A-5}$$

$$\frac{1}{\overline{\rho}^x}\overline{h^x}\delta_x p = \left(h_{i+1,j,k,n} + h_{i,j,k,n}\right)\left(p_{i+1,j,k,n} - p_{i,j,k,n}\right)\Big/$$
$$\left(\rho_{i+1,j,k,n} + \rho_{i,j,k,n}\right) \tag{A-6}$$

$$\left(\frac{1}{\overline{\rho}^{xz}}\tau^{xz}\right)_{k+\frac{1}{2}} = 4\tau^{xz}_{i+\frac{1}{2},j,k+\frac{1}{2},n}\Big/\left(\rho_{i+1,j,k+1,n} + \rho_{i,j,k+1,n} + \rho_{i+1,j,k,n} + \rho_{i,j,k,n}\right) \tag{A-7}$$

$$\left(\frac{1}{\overline{\rho}^{xz}}\tau^{xz}\right)_{k-\frac{1}{2}} = 4\tau^{xz}_{i+\frac{1}{2},j,k-\frac{1}{2},n}\Big/\left(\rho_{i+1,j,k,n} + \rho_{i,j,k,n} + \rho_{i+1,j,k-1,n} + \rho_{i,j,k-1,n}\right) \tag{A-8}$$

$$\delta_x\left\{\left(\overline{\overline{h}^x A_x}^x\right)\delta_x u\right\}_- = \frac{1}{4(\Delta x)^2}\left[\left\{\left(h_{i+2,j,k,n-1} + h_{i+1,j,k,n-1}\right) A_{x_{i+3/2,j,k,n-1}}\right.\right.$$

$$\left.+ \left(h_{i+1,j,k,n-1} + h_{i,j,k,n-1}\right) A_{x_{i+\frac{1}{2},j,k,n-1}}\right\}$$

$$\times \left(u_{i+3/2,j,k,n-1} - u_{i+\frac{1}{2},j,k,n-1}\right)$$

$$- \left\{\left(h_{i+1,j,k,n-1} + h_{i,j,k,n-1}\right) A_{x_{i+\frac{1}{2},j,k,n-1}}\right.$$

$$\left.+ \left(h_{i,j,k,n-1} + h_{i-1,j,k,n-1}\right) A_{x_{i-\frac{1}{2},j,k,n-1}}\right\}$$

$$\times \left(u_{i+\frac{1}{2},j,k,n-1} - u_{i-\frac{1}{2},j,k,n-1}\right) \qquad \text{(A-9)}$$

$$\delta_y\left\{\left(\overline{\overline{h}^x A_y}^y\right)\delta_y u\right\}_- = \frac{1}{4(\Delta y)^2}\left[\left\{\left(h_{i+1,j+1,k,n-1} + h_{i,j+1,k,n-1}\right) A_{y_{i+\frac{1}{2},j+1,k,n-1}}\right.\right.$$

$$\left.+ \left(h_{i+1,j,k,n-1} + h_{i,j,k,n-1}\right) A_{y_{i+\frac{1}{2},j,k,n-1}}\right\}$$

$$\times \left(u_{i+\frac{1}{2},j+1,k,n-1} - u_{i+\frac{1}{2},j,k,n-1}\right)$$

$$- \left\{\left(h_{i+1,j,k,n-1} + h_{i,j,k,n-1}\right) A_{y_{i+\frac{1}{2},j,k,n-1}}\right.$$

$$\left.\left.+ \left(h_{i+1,j-1,n-1} + h_{i,j-1,k,n-1}\right) A_{y_{i+\frac{1}{2},j-1,k,n-1}}\right\}\right.$$

$$\left.\times \left(u_{i+\frac{1}{2},j,k,n-1} - u_{i+\frac{1}{2},j-1,k,n-1}\right)\right] \qquad \text{(A-10)}$$

REFERENCES

1. Neumann, G., "Wind Stress on Water Surface," *Bull. A. M. S.*, Vol. 37, 1956, p. 211.

2. Miles, J. W., "A Note on the Interaction between Surface Waves and Wind Profiles," *J. Fluid Mech.*, Vol. 13, 1965, pp. 433-448.

3. Phillips, O. M., *The Dynamics of the Upper Ocean*, Cambridge University Press, London, 1966.

4. Stewart, R. W., "The Wave Drag of Wind over Water," *J. Fluid Mech.*, Vol. 10, 1966, pp. 189-194.

5. Eckart, C., "The Equations of State of Water and Sea Water at Low Temperatures and Pressures," *American J. of Science*, Vol. 256, April 1958, pp. 225-240.

6. Leendertse, J. J., *A Water-Quality Simulation Model for Well Mixed Estuaries and Coastal Seas: Vol. I, Principles of Computation*, The Rand Corporation, RM-6230-RC, February 1970.

7. Shuman, F. G., "Numerical Experiments with the Primitive Equations," *Proc. International Sym. on Numerical Weather Prediction, Tokyo, Nov. 1960*, Meteorological Society of Japan, 1962, pp. 85-107.

8. Brown, G. D., C. H. Bush, and R. A. Berman, *The Integrated Graphics System for the S-C 6040: Vol. I, User's Manual*, The Rand Corporation, RM-5660-PR, December 1968.

9. Neumann, G., and W. J. Pierson, *Principles of Physical Oceanography*, Prentice-Hall Inc., Englewood Cliffs, New Jersey, 1966.

10. Leendertse, J. J., *The Behavior of the Water-Quality Simulation Model*, The Rand Corporation, P-4810, April 1972.

11. Grammeltvedt, Arne, "A Survey of Finite-Difference Schemes for the Primitive Equations for a Barotropic Fluid," *Mon. Weather Rev.*, Vol. 97, No. 5, May 1969, pp. 384-404.

12. Leendertse, J. J., *Aspects of a Computational Model for Long-Period Water-Wave Propagation*, The Rand Corporation, RM-5294-PR, May 1967.

13. Lilly, D. K., "On the Computational Stability of Numerical Solutions of Time-Dependent Non-Linear Geophysical Fluid Dynamic Problems," *Mon. Weather Rev.*, Vol. 93, No. 1, January 1965, pp. 11-26.

14. Arakawa, A., "Computational Design for Long-Term Numerical Integration of the Equations of Fluid Motion: I. Two-Dimensional Incompressible Flow," *Journal of Computational Physics*, Vol. 1, No. 1, Academic Press, New York, August 1966, pp. 119-143.